INTERNATIONAL JOURNAL FOR NUMERICAL METHODS IN FLUIDS, VOL. 10. 47–77 (1990)

GALERKIN FINITE ELEMENT SIMULATION OF CONVECTION DRIVEN BY ROTATION AND GRAVITATION

FOLUSO LADEINDE* AND K. E. TORRANCE

Sibley School of Mechanical and Aerospace Engineering, Upson Hall, Cornell Univeristy, Ithaca, NY 14853, U.S.A

SUMMARY

The performance of the Galerkin finite element method when applied to time-dependent convection involving rotation, self-gravitation and the normal gravity field in a horizontal cylinder is discussed in this paper. The governing equations, the parameters of the problem and our implementation of the numerical schemes are presented. The accuracy, spatial scale of resolution, flexibility and robustness of the resulting code show the element method as a valuable tool for research in this area or in related problems in astrophysical fluid dynamics. The numerical difficulties in large-amplitude flows are associated with an error-control scheme for time integration and the 'short-time' wiggles in transient Dirichlet problems. Coarse grids give the correct qualitative picture in most simulations, but the type of solution at short time (and hence grid refinement) presumably resolves the degeneracy in the azimuthal orientation of convection cells in flows driven by self-gravitation and (perhaps) centrifugal buoyancy. The final state in transient flows is a motionless isothermal fluid. However, residual motions can be nullified only in the limit of zero grid size in flows driven by centrifugal buoyancy (self-gravitation), while a fairly coarse grid is sufficient for this purpose in normal gravity-driven flows.

KEY WORDS. Finite element Convection Centrifugal Gravitation Cylinder

1. INTRODUCTION

The present study pertains to an application of the finite element method to the simulation of a time-dependent thermal convection problem involving rotation, self-gravitation and the normal external gravity field. The original study of the problem by Ladeinde[1] represents an attempt at providing the needed engineering data for the design of an optimized manufacturing system for thermal processing of fluids enclosed in horizontal cylinders rotating about their axes in a normal gravity field. The model system is shown in Figure 1. Self-gravitation within the cylinder represents a limiting case of the rotating problem.

The initial state in the system is a motionless fluid isothermal at room temperature. The contained fluid is spun up[2] to establish a rigid body rotation. Thereafter the fluid undergoes a transient motion as the wall of the cylinder is heated by maintaining the wall at a high temperature. The final state in the system is motionless fluid isothermal at the new wall temperature. The cause of the transient motion is the combined action of the normal gravitational

* Present address: Fluid/Aerodynamicist, Technalysis Inc., 7120 Waldemar Drive, Indianapolis, IN 46268, U.S.A.

0271–2091/90/010047–31$15.50
© 1990 by John Wiley & Sons, Ltd.
Received 31 October 1988
Revised 11 April 1989

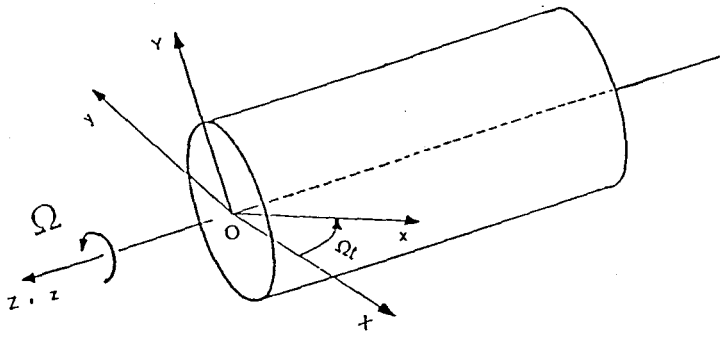

Figure 1. Model rotating system for analysis, showing the inertial (X, Y, Z) and rotating (x, y, z) co-ordinate frames

force field and the centrifugal force field on the density variations associated with temperature variations—essentially the well known fact that hot fluid 'rises'.

Motion driven by normal gravity in a horizontal cylinder has been studied experimentally[3–5] and by finite difference calculations in an inertial co-ordinate frame.[6–9] Thus we know the types of flow behaviour and temperature field to expect from numerical calculations of normal gravity-driven flows in an inertial co-ordinate frame.

However, in the present study, the co-ordinate frame is chosen to rotate with the cylinder in order to explicitly introduce the centrifugal and Coriolis force fields. The normal gravity field is oscillatory in this co-ordinate frame. In terms of finite element implementation, the oscillation of the gravity field requires only a trivial modification of the buoyancy term of the momentum equation; or in fact, merely changing the value of an input parameter in the code. However, when the period is small, the oscillation of the normal gravity field introduces some difficulties in the temporal integration of the governing equations because the timescale of interest (i.e. for heat-up) is orders of magnitude larger than the period of oscillation of the gravity field, and the solution within a period of oscillation must be accurately obtained for an acceptable overall accuracy of the time integration.

We have used the predictor–corrector time integration error-control scheme devised by Gresho *et al.*,[10] since otherwise we do not know the accuracy to which the equations must be solved within a period of oscillation in order to obtain an acceptable overall accuracy. With the error-control scheme the largest step size which ensures a preset accuracy is used by the program. Note that (in numerical schemes without an error control) an arbitrarily large time step size (within a period of oscillation) simulates the false situation in which the normal gravity field is oscillatory in a laboratory frame of reference!

Concerning centrifugal buoyancy, we remark that, at the beginning of the studies, our knowledge of centrifugally driven flow in a horizontal cylinder was inadequate for us to assess the accuracy of the initial numerical results. We are not aware of any previous studies (experimental, analytical or numerical) on centrifugally driven thermal convection in a horizontal cylinder. In fact a lot of difficulty would be encountered in an experimental investigation of rotating systems located on the surface of the Earth. That is, methods must be devised to nullify the effects of the ubiquitous normal gravity field, since otherwise it contaminates the results (see Hart *et al.*[11] for pertinent discussions). Also, an analytical study is very difficult for transient centrifugally driven flow. We are thus left with numerical methods for the calculation of large-amplitude flows.

In a previous study, however, we carried out an analytical study on the related problem of thermal convection in an internally heated self-gravitating cylinder.[1] The purpose of the study on

self-gravitation was to provide a theoretical basis and validate our code for the more difficult transient centrifugally driven flow. A study of self-gravitation is also of intrinsic academic interest. The studies mentioned above used classical mathematical techniques[12] to investigate the instability of the basic fluid state to non-axisymmetric perturbations. The results of the instability analysis were reproduced with the computer code discussed in this paper, and numerically extended to finite amplitude flows.

We have expressed that self-gravitation in the cylinder simulates a limiting behaviour of the rotating case in the foregoing discussion. As we show later in this paper, the difference between the governing equations for convection driven by self-gravitation and the governing equations for convection driven by centrifugal force is the sign of a parameter in the equations. (Readers who are not familiar with the astrophysical concept of self-gravitation or the appropriate expression for a horizontal cylinder might want to consult Tsuboi.[13]) Note, however, that the surface of the cylinder is cooled in the self-gravitation problem to represent a sink for the volumetrically generated heat, while the cylinder wall is heated in the transient rotation problem. The foregoing analogy between self-gravitation and centrifugal force bears some resemblance to that used by Busse and Carrigan[14] in the laboratory simulation of convection processes in stars and planets.

The primary dependent variables are the velocities and temperature (i.e. u, v, w and T). The secondary dependent variables are the streamfunction ψ, the vorticity ζ, the pressure p and the Nusselt number Nu. The secondary variables are obtained by 'processing' the solutions for the primary variables. The governing equations and our implementation of the various finite element schemes for the solution of the governing equations are discussed for both the primary and secondary variables in succeeding sections of this paper. Sample results, code validation and comparison of results with previously published reports are presented, as are the major computational difficulties encountered in large-amplitude flows.

Concluding remarks and appendices describing the element matrices and defining the notation are presented at the end of the paper.

2. MATHEMATICAL FORMULATION

2.1. *Governing equations*

The model of interest in this paper is shown in Figure 1. In this model a horizontal cylinder with axis parallel to the z-axis, or $\mathbf{k}$, rotates at a constant angular velocity $\Omega = \Omega\mathbf{k}$ about its axis in a normal gravity field. Two co-ordinate systems are shown in Figure 1. The co-ordinate system (X, Y, Z) with origin at O is the inertial (non-rotating) co-ordinate frame. The co-ordinate system (x, y, z), also with origin at O, rotates at the container angular velocity $\Omega\mathbf{k}$ and is referred to as the rotating co-ordinate frame. The self-gravitating force field is radially directed towards the centre, while the centrifugal force field is radially directed outwards from the centre. The normal gravity field is unidirectional, pointing downwards in the inertial co-ordinate frame but oscillating in the rotating frame. A two-dimensional simulation in the (r, θ) co-ordinates of the cylinder is carried out here, since this represents a good approximation for this system because of the parameter range studied and the dynamic constraints introduced by rotation (see Busse[15] for pertinent details). Moreover, the cost of time-dependent three-dimensional simulation is prohibitive for the present (oscillating) flow problem.

The governing equations for the motion of an incompressible viscous fluid are those stating the conservation of mass, momentum and energy. For the system shown in Figure 1, these equations, in Cartesian tensor notation, are[1]

$$u_{j,j} = 0 \tag{1}$$

$$\dot{u}_i + u_j u_{i,j} + A\varepsilon_{ijk}\delta_{j3}u_k + BTx_i + p_{,i} + C_i' T - D(\pi(u_{i,j} + u_{j,i})_{,j}) = 0, \tag{2}$$

$$\dot{T} + u_j T_{,j} - T_{,jj} - H = 0. \tag{3}$$

The dot indicates partial differentiation with respect to time, and a comma followed by an index indicates partial differentiation with respect to the spatial co-ordinates indicated by the index. ε_{ijk} is the permutation symbol (pseudo-tensor) and δ_{ij} is the Kronecker delta. The parameters of the system are defined as follows:

$$A = RePr,$$

$$B = Ra_r Pr,$$

$$\mathbf{C}' = \begin{Bmatrix} -E \\ -G \end{Bmatrix},$$

$$D = Pr,$$

$$E = E(t) = RaPr \sin(RePrt/2),$$

$$G = G(t) = RaPr \cos(RePrt/2),$$

$$\mathbf{x} = (x, y, 0)^*,$$

where

$Re = 2R^2\Omega/\nu$ = rotational Reynolds number (or square root of Taylor number Ta)

$Pr = \nu_0/\alpha$ = Prandtl number,

$Ra_r = Rg'\beta\overline{\Delta T}R^3/\nu\alpha$ = rotational or self-gravitating Rayleigh number,

$Ra = g\beta\overline{\Delta T}R^3/\nu\alpha$ = normal gravity Rayleigh number.

In addition, the non-dimensional viscosity $\pi = \nu/\nu_0$ appears, which requires a specifying equation. Also note that:

$$\overline{\Delta T} = \begin{cases} T_w - T_0 & \text{transient heating problem,} \\ Q'''R^2/k & \text{internal heat generation problem,} \end{cases}$$

$$H = \begin{cases} 0 & \text{transient heating problem,} \\ 1 & \text{internal heat generation problem,} \end{cases}$$

$$g' = \begin{cases} \Omega^2 & \text{rotation problem,} \\ -2\pi\rho_0 G & \text{self-gravitation problem.} \end{cases}$$

R, ν, α, β and g are the radius of the cylinder, the kinematic viscosity of the fluid (with a reference value of ν_0), the thermal diffusivity, the volumetric expansion coefficient and the normal gravity respectively. T_w and T_0 are the wall temperature and a reference temperature respectively, the latter being taken as the initial temperature in the system. Q''' and k are the dimensional uniform heating rate and the thermal conductivity respectively, while G is the gravitational constant.

Note that the Boussinesq approximation has been used in the derivation of equation (2). Also the pressure that appears in equation (2) is the reduced pressure which is given by

$$p = \frac{R^2}{\rho_0 \alpha^2}[P - \tfrac{1}{2}\rho_0 g'(x^2 + y^2) + \rho_0 g(x \sin \Omega t + y \cos \Omega t)], \tag{4}$$

where P is the dimensional total pressure and p is the non-dimensional reduced pressure, which is due wholly to fluid motion. Furthermore, the term $A\varepsilon_{ijk}\delta_{j3}u_k$ can be removed from equation (2) by

further redefining the pressure.[1] The term represents a residual of the divergence of velocity in a dynamic sense (e.g. via the vorticity equation), and the deviation from zero is a measure of the error caused by a penalization of the incompressibility constraint. We have thus retained the term to find out the values of $RePr$ that give acceptable solutions. The results presented in this paper are from simulations with negligible continuity residual.

2.2. *Initial and boundary conditions*

The initial condition is

$$\mathbf{u}=(u, v, T)^*=0, \tag{5}$$

the condition on the surface of the cylinder is $u=v=0$, and

$$T=\begin{cases}1 & \text{transient heating problem,}\\ 0 & \text{internal heat generation problem.}\end{cases}$$

The Stokes streamfunction ψ and z-component of vorticity, ζ, can be obtained in both inertial and rotating co-ordinate frames from the relation

$$\zeta=\frac{1}{r}\frac{\partial}{\partial r}(ru_\theta)-\frac{1}{r}\frac{\partial u_r}{\partial\theta}+\lambda RePr=-\Delta\psi, \tag{6a}$$

where

$$u_r=\frac{1}{r}\frac{\partial\psi}{\partial\theta}, \qquad u_\theta=-\frac{\partial\psi}{\partial r},$$

$$\Delta\equiv\frac{\partial^2}{\partial r^2}+\frac{1}{r^2}\frac{\partial^2}{\partial\theta^2}+\frac{1}{r}\frac{\partial}{\partial r},$$

$$\lambda=\begin{cases}0 & \text{rotating co-ordinate frame,}\\ 1 & \text{inertial co-ordinate frame.}\end{cases}$$

3. FINITE ELEMENT SOLUTION

The consistent (not the reduced integration) penalty Galerkin finite element method with a time integration error control has been used for the solution of the governing equations for the primary dependent variables. The penalty formulation requires special treatments of the continuity equation and the pressure terms of the momentum equation. The continuity equation for the penalized system is

$$u_{j,j}+\varepsilon' p=0, \tag{6b}$$

where ε' is the penalty parameter.

Following standard finite element procedures (e.g. Gresho[16]) we obtain the weak forms of the continuity equation in (6b), the nth component of the momentum equation, and the energy equation as

$$\int_\Omega \psi_i' u_{j,j}\,d\Omega+\varepsilon'\int_\Omega \psi_i' p\,d\Omega=0, \tag{7a}$$

$$\int_\Omega \phi_i \dot{u}_n \mathrm{d}\Omega + \int_\Omega \phi_i u_j u_{n,j} \mathrm{d}\Omega + A \int_\Omega \phi_i \varepsilon_{njk} \delta_{j3} u_k \mathrm{d}\Omega + B \int_\Omega \phi_i T x_n \mathrm{d}\Omega$$
$$+ \int_\Omega \phi_i C_n' T \mathrm{d}\Omega - \int_\Omega \phi_{i,n} p \mathrm{d}\Omega + D \int_\Omega \phi_{i,j} (\pi u_{n,j} + \pi u_{j,n}) \mathrm{d}\Omega$$
$$= -\int_S \phi_i \eta_n p \mathrm{d}S + D \int_S \phi_i \eta_j (\pi u_{n,j} + \pi u_{j,n}) \mathrm{d}S \equiv \int_S \phi_i t_n \mathrm{d}S, \tag{7b}$$

$$\int_\Omega \phi_i \dot{T} \mathrm{d}\Omega + \int_\Omega \phi_i u_j T_{,j} \mathrm{d}\Omega + \int_\Omega \phi_{i,j} T_{,j} \mathrm{d}\Omega = \int_S \phi_i \eta_j T_{,j} \mathrm{d}S + \int_\Omega \phi_i H \mathrm{d}\Omega \equiv \int_S \phi_i q \mathrm{d}S + \int_\Omega \phi_i H \mathrm{d}\Omega. \tag{8}$$

The definition of t_n and q is obvious from the identities defined in equations (7) and (8). t_n and q are supplied via a specified stress and heat flux condition (natural boundary conditions) on the bounding surface S of the domain Ω. ψ_i' is any of the pressure basis functions and ϕ_i in (7) and (8) is any of the velocity (or temperature) basis functions. The appropriate expansions into the finite-dimensional piecewise polynomial basis sets are

$$u_\lambda = \sum_{j=1}^{N} u_\lambda^j(t) \phi_j(\mathbf{x}), \tag{9}$$

$$T = \sum_{j=1}^{N} T^j(t) \phi_j(\mathbf{x}), \tag{10}$$

where $\lambda = 1, 2$ for the two velocity components, $\mathbf{x} = (x, y)^*$, and u_λ^j and T^j are the respective values of u_λ and T at the velocity (temperature) node j. The formulation is Galerkin because the same functions $\boldsymbol{\phi}$ are used as test functions and for the interpolation of the dependent variables.

The pressure $p^{(e)}$ within an element is allowed to vary linearly according to

$$p^{(e)} = \sum_{j=1}^{3} p^j(t) \psi_j'(\mathbf{x}), \tag{11}$$

where p^j is the value of the pressure at the jth pressure 'node' and ψ_j' is the corresponding basis function for interpolating pressure. With this formulation the pressure is discontinuous at element boundaries. Following Engelman *et al.*[17] the pressure basis functions are chosen to be in the global space $(1, x, y)$, so that within an element we have

$$p^{(e)} = p_1 + p_2 x + p_3 y. \tag{12}$$

At the element level the spatial co-ordinates x and y are interpolated according to

$$x = \sum_{k=1}^{L} x^k \phi_k'(\mathbf{x}), \tag{13}$$

$$y = \sum_{k=1}^{L} y^k \phi_k'(\mathbf{x}), \tag{14}$$

where x^k and y^k are the respective values of x and y at any element node k chosen for co-ordinate transformation, and the ϕ_k' are the interpolation functions for co-ordinate transformation. As we discuss shortly, we have chosen ϕ' *different* from ϕ in the present formulation.

Using the relationships in (9)–(14), the matrix quations corresponding to equations (7) and (8) are

$$\int_\Omega \psi_i' \phi_{j,n} \mathrm{d}\Omega u_n^j + \varepsilon' \int_\Omega \psi_i' \psi_j' \mathrm{d}\Omega p^j = 0, \tag{15a}$$

$$\int_\Omega \phi_i\phi_j \mathrm{d}\Omega \dot{u}_n^j + \int_\Omega \phi_i(u_{\alpha l}\phi_l)\frac{\partial \phi_j}{\partial x_\alpha}\mathrm{d}\Omega u_n^j + A\int_\Omega \phi_i \varepsilon_{n\alpha k}\delta_{\alpha 3}\phi_j \mathrm{d}\Omega u_k^j + B\int_\Omega \phi_i\phi_j(x_{\mu n}\phi'_\mu)\mathrm{d}\Omega T^j$$
$$-\int_\Omega \phi_{i,n}\psi'_j \mathrm{d}\Omega p^j + \int_\Omega \phi_i C'_n \phi_j \mathrm{d}\Omega T^j + D\int_\Omega \frac{\partial \phi_i}{\partial x_\alpha}\pi\frac{\partial \phi_j}{\partial x_\alpha}\mathrm{d}\Omega u_n^j + D\int_\Omega \frac{\partial \phi_i}{\partial x_\alpha}\pi\frac{\partial \phi_j}{\partial x_n}\mathrm{d}\Omega u_\alpha^j$$
$$= \int_S \phi_i t_n \mathrm{d}S, \tag{15b}$$

$$\int_\Omega \phi_i\phi_j \mathrm{d}\Omega \dot{T}^j + \int_\Omega \phi_i(u_{\alpha l}\phi_l)\frac{\partial \phi_j}{\partial x_\alpha}\mathrm{d}\Omega T^j + \int_\Omega \frac{\partial \phi_i}{\partial x_\alpha}\frac{\partial \phi_j}{\partial x_\alpha}\mathrm{d}\Omega T^j = \int_S \phi_i q \mathrm{d}s + \int_\Omega \phi_i H \mathrm{d}\Omega, \tag{16}$$

where $i, j, l = 1, 2, \ldots, N$, $\alpha, k = 1, 2$ and $\mu = 1, 2, \ldots, L$.

We have used a Lagrange element consisting of a nine-node biquadratic interpolation for velocity (temperature) and a three-node discontinuous interpolation for pressure. The shape functions of the eight-node serendipity element have been used to map the geometry of the nine-node element. No significant error was expected (or observed) by this procedure since it is well known that both the nine-node Lagrange element and the eight-node serendipity element have identical boundary shape function.[18] Thus, at the element level, the range of the summation indices in equation (9) or (10) is nine while that in equation (13) or (14) is eight.

If we substitute for the nodal values of pressure (p^j) that appear in the discretized momentum equation (15b) by using (15a) we will see that the contribution of the pressure terms to the discretized nth component of the momentum equation (other than the contribution to t_n) is

$$\varepsilon' C_{ij}^n [O_{\beta j}]^{-1} C_{\beta\alpha}^{1*} u_\alpha + \varepsilon' C_{ij}^n [O_{\beta j}]^{-1} C_{\beta\alpha}^{2*} v_\alpha,$$

where $i, \alpha = 1, 2, \ldots, 9$, $j, \beta = 1, 2, 3$ and $n = 1, 2$; ε' is the penalty parameter,

$$C_{ij}^n = \int_\Omega \frac{\partial \phi_i}{\partial x_n}\psi'_j \mathrm{d}\Omega = C_{ji}^{n*}, \qquad O_{\alpha\beta} = \int_\Omega \psi'_\alpha \psi'_\beta \mathrm{d}\Omega$$

and u_α and v_α are the values of u and v at the αth node of an element. Values between 10^6 and 10^{10} have been used for the penalty parameter ε', depending on the magnitude of the flow parameter.

The spatially discretized Galerkin finite element equations can be written as

$$\mathbf{M}\dot{\mathbf{u}} + \mathbf{K}(u, v, \varepsilon')\mathbf{u} = \mathbf{f}, \qquad \mathbf{u}(0) = \mathbf{u}_0, \tag{17}$$

where $\mathbf{u}$ is the vector of nodal points of u, v and T, and $\mathbf{K}$ contains, among other things, the non-linear convective terms, the penalty terms and the viscous and thermal diffusion terms. $\mathbf{f}$ contains information on flux (kinematic and thermal) boundary conditions and the volumetric heating.

The methods we have used for the time integration of equation (17) include those in which time steps are held fixed throughout the integration period and those in which time truncation error estimates are used to vary the step sizes in such a way that a given level of (time integration) accuracy is assured even if the time step size becomes quite large. The time step size is determined by the physics of the flow in this time integration scheme. The scheme has been discussed in detail by Gresho *et al.*[10]

We have used the backward Euler and the trapezoid rule for the constant-step-size integrations. However, all the results presented in the present paper were obtained with the error-control scheme. For the error-control scheme the solution at the end of a time step is predicted with the variable-step, second-order Adams–Bashforth (AB) formulae, or

$$\mathbf{u}_p^{l+1} = \mathbf{u}^l + \frac{\Delta t^l}{2}\left[\left(2 + \frac{\Delta t^l}{\Delta t^{l-1}}\right)\dot{\mathbf{u}}^l - \frac{\Delta t^l}{\Delta t^{l-1}}\dot{\mathbf{u}}^{l-1}\right], \tag{18}$$

where l denotes time level, Δt is the step size and the subscript 'p' denotes 'predictor'. The predicted solution is corrected by integration with the implicit, non-dissipative, completely stable, second-order trapezoid rule. When applied to the system in equation (17) the trapezoid rule is

$$\left[\frac{2}{\Delta t^l}\mathbf{M}+\mathbf{K}(\mathbf{u}^{l+1})\right]\mathbf{u}^{l+1}=\frac{2}{\Delta t^l}\mathbf{M}\mathbf{u}^l+\mathbf{f}^l+\mathbf{f}^{l+1}-\mathbf{K}(\mathbf{u}^l)\mathbf{u}^l. \tag{19}$$

We specify a maximum local time integration error tolerance ε_0 so that the next time step size which ensures this accuracy is given by

$$\Delta t^{l+1}=\Delta t^l\left(\frac{\varepsilon_0}{\|d^{l+1}\|}\right)^{1/3}, \tag{20}$$

where

$$d^{l+1}=\frac{\mathbf{u}^{l+1}-\mathbf{u}_{\mathrm{p}}^{l+1}}{3(1+\Delta t^{l-1}/\Delta t^l)}+\text{higher-order terms}.$$

The details of the foregoing scheme, including the norm defined for $\|\bullet\|$, etc., can be found in the literature. We have used a value of $\varepsilon_0=0{\cdot}002$ for all simulations with the error-control scheme.

The Newton–Raphson procedure has been implemented for linearizing equation (19). The linearized system is

$$\left[\frac{2}{\Delta t^l}\mathbf{M}+\mathbf{K}(\mathbf{u}_m^{l+1})+\mathbf{N}'(\mathbf{u}_m^{l+1})\right]\Delta\mathbf{u}_m^{l+1}=\frac{2}{\Delta t^l}\mathbf{M}\mathbf{u}^l+\mathbf{f}^l+\mathbf{f}^{l+1}-\mathbf{K}(\mathbf{u}^l)\mathbf{u}^l-\left[\frac{2}{\Delta t^l}\mathbf{M}+\mathbf{K}(\mathbf{u}_m^{l+1})\right]\mathbf{u}_m^{l+1}, \tag{21}$$

so that

$$\mathbf{u}_{m+1}^{l+1}=\mathbf{u}_m^{l+1}+\Delta\mathbf{u}_m^{l+1}. \tag{22}$$

The subscript m denotes the iterations within a time step. The matrices in equation (21) are written out in full in Appendix I, along with the integrals involved. All integrals, including those containing the penalty parameter, were evaluated at 3×3 Gauss points.

The results given in equation (21) were derived for the trapezoid rule. For the backward Euler the following adjustments to equation (21) are necessary:

$$\frac{2}{\Delta t^l}\to\frac{1}{\Delta t^l},\qquad \mathbf{K}(\mathbf{u}^l)\mathbf{u}^l\to 0,\qquad \mathbf{f}^l\to 0.$$

For the steady state version of the code we have

$$\frac{2}{\Delta t^l}\to 0,\qquad \mathbf{K}(\mathbf{u}^l)\mathbf{u}^l\to 0,\qquad \mathbf{f}^l+\mathbf{f}^{l+1}\to\mathbf{f}.$$

We have also weighted iteration values of $\mathbf{u}$ in order to accelerate the convergence of steady state calculations:

$$\mathbf{u}=(1-\alpha)\mathbf{u}_m+\alpha\mathbf{u}_{m+1},$$

where a value of 0·67 has been used for α in most steady state calculations. Also, a continuation process has been implemented for steady state calculations involving relatively high parameter values. The iteration (or steady state) convergence criterion used is

$$\left[\sum_{i=1}^{3M}\left(\frac{u_i^{n+1}-u_i^n}{u_i^n}\right)^2\right]^{1/2}<0{\cdot}01,$$

where n is the iteration or time level, M is the total number of nodes in the mesh and u_i is u, v or T.

3.1. *Penalty transient*

An implicit scheme must be used for a cost-effective time integration with the penalty method. In addition, the penalty parameter introduces considerable stiffness to the system shown in equation (17) or (21). The stiffness problem associated with a related system has been studied by Sani *et al.*[19] and Sani.[20] Based on the findings by Sani, a time integration which starts out with a dissipative scheme is required to severely damp out the unphysical high-frequency components at short time. We started the time integrations in the present study with three (corrector) steps of backward Euler. The integration was then completed with either the backward Euler or the trapezoid rule, with or without error control.

3.2. *Condensation of internal degrees of freedom*

We have implemented a condensation procedure whereby the degrees of freedom associated with the centre node of each element are removed prior to assembly. This was done to reduce the bandwidth of the assembled equations. A small bandwidth is desirable for the in-core skyline solution method employed in the present analysis.

We note that because the element matrix is unsymmetric we cannot benefit from the efficient static condensation algorithm of Wilson.[21] However, we have considerably simplified the condensation procedure for unsymmetric matrices. If we denote the original element square matrix by S, where the elements of S are arranged such that the equations corresponding to the centre node degrees of freedom are contained in the bottom rows of S, then the elements of the condensed matrix can be written as

$$S(i,j)=S(i,j)-\left[\sum_{m=1}^{N1-N2}\left(\sum_{k=1}^{N1-N2}S(i,N2+k)X_{km}\right)S(m+N2,j)\right],$$

where $i,j=1,2,\ldots,N2$; $N1$ is the initial size of element matrix S (27 in the present problem), $N2$ is the size of the element matrix S after condensation (24 in the present problem) and X is the inverse of the element submatrices associated with the centre nodes. Similarly the condensed right-hand side F is

$$F(i)=F(i)-\left[\sum_{m=1}^{N1-N2}\left(\sum_{k=1}^{N1-N2}S(i,N2+k)X_{km}\right)F(m+N2)\right],$$

where $i=1,2,\ldots,N2$. The solution at the centre nodes can easily be retrived after solving for the element boundary nodes. It is readily shown that the solution for the variables associated with element centre node is given by

$$U(N2+i)=X_{ij}f_j,\quad i,j=1,2,\ldots,N1-N2,$$

where

$$f_j\doteq F(N2+j)-\sum_{k=1}^{N2}S(N2+j,k)\,U(k)$$

and U represents the nodal values of **u**.

3.3. *Calculation of secondary flow variables*

The streamfunction was calculated by direct finite element discretization of the relation given in equation (6a). We have used the so-called global smoothening technique described by Lee *et al.*[22] for calculating the nodal values of vorticity and pressure, while the consistent heat flux

method[23, 24] has been used for calculating the Nusselt number. A fairly complete account of our implementation of these schemes is given in Ladeinde.[1]

3.4. Computation grids

The grids we have used for the calculations are given in Figure 2. The grids have been referred to as S593, G201, G449 and G649, where the 'S' stands for 'streamline' mesh (after Bercovier *et al.*[25]) and the 'G' stands for 'general' mesh. The number 593, for example, refers to the total number of nodal points in the mesh, including nodes at element centroids. The general mesh is preferred because, with our modest mesh generation routine, elements are concentrated (i.e. waisted) at the centre when the streamline mesh is generated, and it is cumbersome to obtain comparable number of elements in the azimuthal and radial directions with the streamline mesh. The latter problem is very serious at the wall, and the computed wall heat flux is grossly in error. Also, the fewer number of elements on the boundary means more unknowns, since our code deletes equations corresponding to specified (i.e. Dirichlet) boundary conditions. A satisfactory element distribution is obtained with the general mesh. The two meshes gave identical solutions for several test problems, although more elements were required with the streamline mesh. All the computations reported in this paper have been done with the general mesh. More information on the general meshes is provided in Table I, since they are useful for the discussions provided in subsequent sections of this paper.

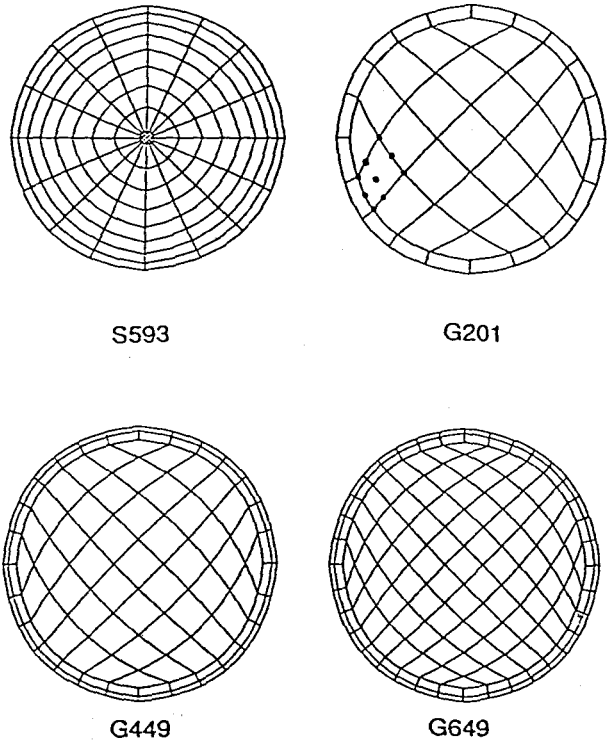

Figure 2. The grids employed for calculations. The nomenclature for the grids is defined in the text. Nine-node Lagrange elements are used for all computations reported in this paper

Table I. Other details of the grids used for computation

Property	Grids G201	G449	G649
Number of elements	45	105	153
Number of boudnary nodes for boundary condition specification and for heat flux calcuation	40	56	72
Total number of nodes	201	449	649
Number of primary degrees of freedom per node	3	3	3
Total number of unknown primary variables	603 (or 201 × 3)	1347	1947
Total number of Dirichlet boundary conditions for primary variables	120 (or 40 × 3)	168	216
Number of unknowns after removal of primary varibles with Dirichlet boundary conditions	483 (or 603–120)	1179	1731
Total number of unknown secondary variables (ψ, ζ, p, Nu): variables are not coupled	(3 × 201) + 40 (for Nu)	(3 × 449) + 56	(3 × 649) + 72

4. SAMPLE RESULTS

4.1. Code validation

The computer code developed for the present problem has undergone stringent tests to establish its validity. This was necessary since we are not aware of any previous studies that have combined the schemes discussed above in one code. Some of the test problems are:

(a) Transient heat conduction in an internally heated rectangular box.[26]
(b) Steady state isothermal flow on a curved channel, $R = 100$.[27] The Reynolds number R is $(Pr)^{-1}$ in the present formulation.
(c) Flow over a rectangular step, $R = 200$.[28]
(d) Steady state isothermal flow in a lid-driven cavity, $R = 100$.[29]
(e) Steady or quasi-steady state normal gravity-driven thermal convection in a horizontal cylinder with applied temperature gradient (including cosine forms) or volumetric heat generation, $10^3 \leq Ra \leq 10^6$.[30,31,8]
(f) Transient thermal convection in a rectangular box, $Ra = 10^5$.[32]
(g) Steady state thermal convection in a rectangulr box, $10^3 \leq Ra \leq 10^6$.[33–35]
(h) Critical Rayleigh number and most unstable wave number for the onset of flow in an internally heated self-gravitating horizontal cylinder.[1] Other important but trivial tests

involve the reproduction of the analytical conduction temperature profile in the self-gravitating cylinder problem, and the rigid body solution for vorticity and streamfunction as observed in inertial and rotating co-ordinate frames. We also checked the computed period of oscillation of the normal gravity field against the exact value of $4\pi/RePr$ (from equation (2)).

Excellent agreement was observed in all test problems. The test problems in items (e) and (h) are of interest because they have a direct relevance to the present investigation. These cases will be discussed shortly after a brief discussion of Table II where we compare results obtained using our code with the benchmark solutions provided by de Vahl Davis[35] for a comparison exercise suggested by Jones and Thompson.[34] The exercise involves the simulation of natural convection in a square cavity. A horizontal temperature gradient is maintained in the basic state in the cavity by keeping the temperature at the left wall fixed at $T=1$ and that at the right wall at $T=0$. The horizontal walls are insulated and velocities are zero at all walls. A Prandtl number of 0·71 is suggested, while values between 10^3 and 10^6 are used for the Rayleigh number. Diagnostic quantities such as ψ, u_{max}, v_{max}, etc. are compared in Table II. Note that a graded mesh (not shown) consisting of 84 elements with 361 nodal points is used in the present studies, whereas the benchmark solutions were obtained with a finite difference mesh of 61×61 nodal points.

In Figure 3(a) we compare our steady state results for the Nusselt number distribution on the surface of a horizontal cylinder with those obtained by Hellums and Churchill.[30] The initial condition is $u=v=T=0$ at $t=0$ and $u=v=0$ on the boundary, while the boundary condition on the temperature T is

$$T=\begin{cases} 1/2 & \text{at } R=1, \quad 0\leq\theta\leq\pi, \\ -1/2 & \text{at } R=1, \quad \pi\leq\theta\leq 2\pi. \end{cases}$$

The angle θ is measured counterclockwise from the bottom of the cylinder. The parameter values are $Ra=4{\cdot}305\times10^5$ and $Pr=0{\cdot}7$. Hellums and Churchill used a finite difference grid of 11×26 for half the domain, while the flow in the whole domain is simulated (to assess the symmetry of solutions) using the mesh G449 (with 56 nodes for the Nusselt number) in the present calculations. The agreement between the two results is excellent. Note that the finite difference calculation by Hellums and Churchill could not give accurate (finite) values for the Nusselt number at $\theta=0$ and $\theta=\pi$, but that no such difficulty was encountered in the present (consistent) method of calculating the heat flux. The temperature and the quantity $U_\theta=(Pr^{-1})u_\theta$ calculated with our code are also compared with the numerical calculations by Hellums and Churchill and with the results of

Table II. Comparison with benchmark solutions provided by de Vahl Davis[35] for natural convection in a square cavity. The boundary conditions and parameter values are discussed in the text. Note that the benchmark solutions were obtained from a finite difference mesh consisting of 61×61 nodal points, whereas only 84 elements (with 361 nodal points) were used for the present simulation. The reader is reminded that $|\psi|_{max}$ is centrally symmetric about (0·5, 0·5).

	$Ra=10^3$		$Ra=10^5$		$Ra=10^6$	
Quantity	Benchmark	Present	Benchmark	Present	Benchmark	Present
$\lvert\psi\rvert_{mid}$	1·174	1·172	9·111	9·072	16·32	16·30
$\lvert\psi\rvert_{max}$	—	1·172	9·612	9·559	16·750	16·659
(x, y)	—	(0·5, 0·5)	(0·285, 0·601)	(0·69, 0·3733)	(0·151, 0·547)	(0·8167, 0·5)
u_{max} at $x=0{\cdot}5$	3·649	3·642	34·73	34·25	64·63	62·7
y	0·813	0·8167	0·855	0·88	0·850	0·88
v_{max} at $y=0{\cdot}5$	3·697	3·689	68·59	67·45	219·36	219·53
x	0·178	0·183	0·066	0·0765	0·0379	0·042

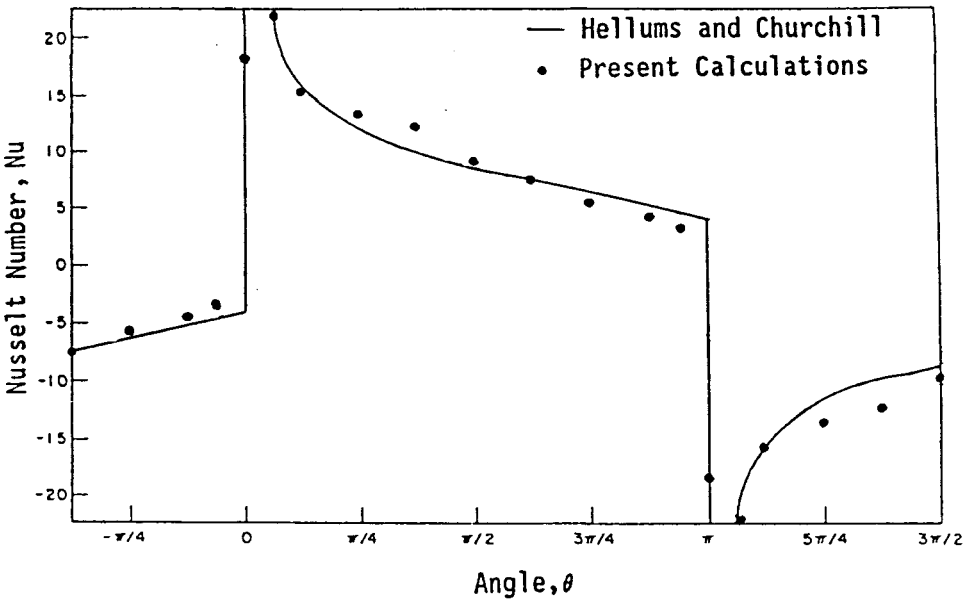

Figure 3(a). Comparison of calculated Nusselt number distribution on the surface of a heated cylinder with those reported by Hellums and Churchill.[30] The consistent heat flux method of Gresho *et al.*[24] was used in the present calculations. Both the 'lumped mass method' and the 'consistent mass method' gave identical results. $Ra = 4{\cdot}305 \times 10^5$, $Pr = 0{\cdot}70$ and θ is measured counterclockwise from the bottom of the cylinder. The boundary conditions are discussed in the text. The angle θ shown in this figure is defined relative to the co-ordinate frame used by Hellums and Churchill. This is not so for all other figures in this paper

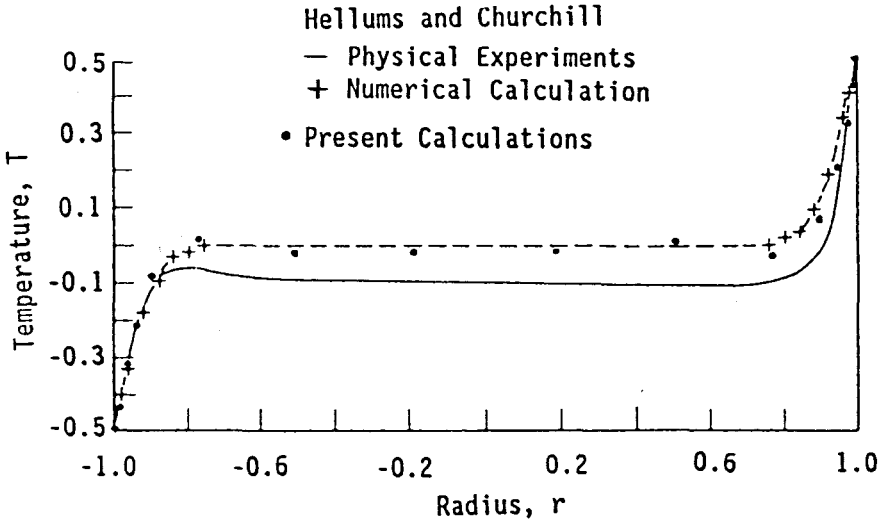

Figure 3(b). Temperature profile along the diameter $\theta = 0$ for natural convection in a horizontal cylinder for the conditions used by Hellums and Churchill.[30] We compare our results with numerical calculations by Hellums and Churchill and with results from physical experiments, also carried out by Hellums and Churchill

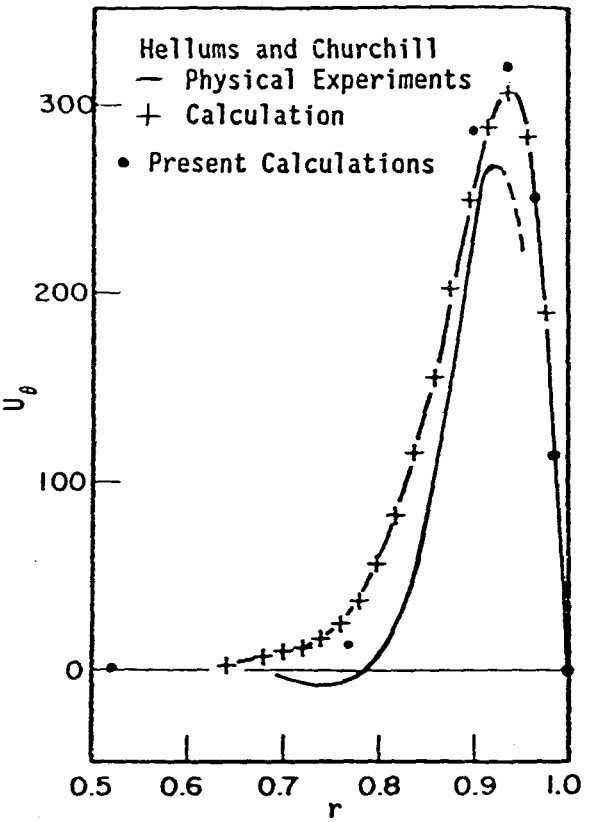

Figure 3(c). The quantity $U_\theta=(Pr^{-1})u_\theta$ along the diameter $\theta=\pi$ for natural convection in a horizontal cylinder for the conditions used by Hellums and Churchill.[30] We compare our results with numerical calculations by Hellums and Churchill and with results from physical experiments, also carried out by Hellums and Churchill

physical experiments, also carried out by Hellums and Churchill (Figures 3(b) and 3(c)). Temperature is calculated along the diameter $\theta=0$, while U_θ is calculated along $\theta=\pi$. (θ here refers to our co-ordinate system, as is always the case unless stated otherwise.)

The new results presented in this paper represent a numerical extension, to finite amplitude, of the analytical treatment of the internally heated self-gravitating cylinder problem. We will also present sample time-dependent solutions for the normal gravity-driven, internal heat generation problem of Van Sant.[6] The latter results will be given in both inertial and rotating co-ordinate frames. Following this we will give a sample result to illustrate the flows observed when self-gravitation and the normal external gravity field are both present in the internally heated cylinder. The above studies are then repeated with surface heating 'replacing' volumetric heat generation, and the centrifugal force field (from rotation) replacing the self-gravitating force field. The normal gravity field plays an identical role to its role in the volumetric heat generation problem.

The simulations in the original study involved Ra values between 0 and 10^6, Ra_r values between 0 and 10^6, and Re values beteen 0 and 250. More than 20 combinations of these three parameters were simulated. The Prandtl number and the dimensionless viscosity were held fixed at 7 and 1 respectively for all calculations. We will discuss sample results from the volumetric heat generation problem first, followed by results from the transient heating problem.

4.2. Sample results from the volumetric heat generation problem

4.2.1. Motion driven by self-gravitation ($Ra = Re = 0$). It is first remarked that the transport of the heat generated within the cylinder is by molecular diffusion before the onset of motion. Under this condition the maximum temperature occurs at the geometric centre with a theoretical value of $T_e(0) = 0{\cdot}25$ and decreases to a value of zero at the wall, or

$$T_e = \frac{1 - r^2}{4}. \tag{23}$$

Thus the isotherms are concentric circles with centre at the orign. The total amount of heat generated within the cylinder is (theoretically) $-\pi$ under quasi-steady state conditions. This heat escapes through the surface at an average wall flux of -0.5. Note that the total (average) heat flux at the wall at quasi-steady state is independent of the strength of motion (Ra_r or Ra) and is always equal to $-\pi\,(-0{\cdot}5)$, although, as we report shortly, the local distribution along the wall is heavily dependent on the strength of fluid motion.

It has been found from previous mathematical analysis[1] that the basic conduction solution (i.e. $u = v = 0$ and equation (23) for temperature) becomes unstable to non-axisymmetric perturbations at $Ra_r = 1{\cdot}3738 \times 10^4$. The instability sets in as direct (non-oscillatory) modes, the most unstable corresponding to an azimuthal wave number of 1 (i.e. a two-cell solution in the (r, θ) plane). These results have been reproduced with the present finite element code. Table III summarizes the results of a numerical simulation carried out for a range of Ra_r values between 0 and 10^6 for the purpose of determining the onset of motion. The strength of motion has been measured with the streamfunction $|\psi|$ and with η, the ratio of maximum temperature at conduction (i.e. $T_e(0)$) to the maximum temperature at a particular Ra_r values (i.e. T_m). We observe from the table that the transport of heat is by conduction for $Ra_r \leq 1{\cdot}4 \times 10^4$.

Table III. Maximum temperature and streamfunction at various Ra_r for the purpose of numerically determining the critical Rayleigh number for flows driven by self-gravitation within a horizontal cylinder[1]

$Ra_r \times 10^{-4}$	T_m	$\eta = T_e(0)/T_m$	One location of T_m	$\lvert\psi\rvert_{max}$
0·0	0·248, 0·25	1, —	(0, 0), (0, 0)	0, 0
0·5	0·248, 0·25	1·000, —	(0, 0), (0, 0)	0·0057, 0·00001
1·2	0·248	1	(0, 0)	0·0145
1·35	0·248	1	(0, 0)	0·0130
1·4	0·248, 0·247	1, —	(0, 0), (0, 0)	0·014, 0·325
1·5	0·246	1·008	(0, 0)	0·746
1·66	0·239	1·038	(−0·127, −0·127)	1·380
2·0	0·231	1·074	(−0·251, 0)	1·728
2·5	0·217	1·143	(−0·372, 0·310)	2·638
3·3	0·197	1·259	(−0·372, 0·130)	3·077
4·0	0·190	1·305	(−0·372, 0·130)	4·524
10·0	0·154, 0·151	1·610, —	(0·381, 0·381) (−0·363, −0·363)	7·706, 8·709
100·0	−, 0·088	—, —	−, (0·470, −0·612)	—, 25·11

In cases where three are two entries the first entry refers to G201 and the second refers to G449. A dash in an entry implies that the particular entry is not of interest or relevant. Note that the actual numbers do not carry much significance since very coarse grids are used. Only the qualitative trend is important. More details are given in the text.

We have provided Figure 4 to show the results obtained from numerical simulation at supercritical Ra_r. We observe from the figures that fluid motion has become quite evident at $Ra_r = 1{\cdot}66 \times 10^4$ as ψ_{max} has increased from the precritical value of zero to approximately 1·3. We also observe that the internally generated heat is more rigorously transported and that the hottest region has moved away from the centre. The foregoing trends have been considerably amplified at $Ra_r = 10^5$.

The distribution of heat flux along the wall is useful design information. However, we have observed that the orientation of the convection cells (and hence the distribution of heat flux on the wall) remained rather arbitrary and could not be determined *a priori* for the supercritical Ra_r values studied. The fact that no azimuthal orientation is preferred is an intrinsic property of the present problem—a property that presumably results from the uniform azimuthal component of the self-gravitation force at any radius. The solution at quasi-steady state is presumably determined by the solution at 'short time'. As we show shortly, the latter problem is not encountered in flows driven by a unidirectional body force (i.e. normal gravity), and the regions of high heat flux and those of low heat flux are known *a priori*. We also remark that the arbitrary azimuthal orientation of convection cell and distribution of wall heat flux cannot be observed in numerical calculations which use only half of the domain (on the assumption of the existence of a symmetry axis). The degeneracy probably takes on a different form under such conditions.

4.2.2. Motion driven by normal gravity in inertial and rotating frames ($Ra_r = 0$). Figures 5 and 6 are provided to illustrate the effect of the choice of co-ordinate frame on motion driven by a normal gravity field in an internally heated horizontal cylinder. The Rayleigh number for both calculations is $Ra = 10^5$. When the governing equations are solved in an inertial frame ($Re = 0$) the flowfield consists of an initially weak two-cell pattern that relaxes into fuller cells as the flow develops. The two-cell convection pattern is a familiar one from the literature.[6,7] The internally generated heat is transported (by upward-moving fluid) to the boundary, where the fluid is cooled and returned to the interior for further heating.

The temporal evolution of the flow is slightly more complicated in a rotating frame. At short times the convection pattern observed in the rotating frame are the same 'kidney beans' (except for the orientation of the beans) observed in an inertial frame. However, as the flow develops the observer in the rotating frame sees one of the cells progressively getting bigger at the expense of the other. At quasi-steady state the observer sees a convection pattern consisting of a large cell with circulation in the clockwise sense and a small countercirculating eddy in one 'corner' of the cylinder. It is pointed out that the flowfield shown in Figure 6 is the one that will be observed in an internally heated horizontal cylinder of fluid rotating about its axis in a normal gravity field. The parameters for the sample case in Figure 6 are $Ra = 10^5$, $Re = 24{\cdot}7$, $Pr = 7$ and $\pi = 1$. The arrows in the figure show the instantaneous direction of the normal gravity field at the time indicated. We emphasize that only streamfunction (and vorticity) values obtained in the same co-ordinate system can be compared; and in the rotating frame we can compare streamfunction (and vorticity) values only in simulations involving the same Re and Pr values.[1]

4.2.3. Motion driven by a combination of self-gravitation and normal gravity field. The solution observed depends on the ratio $F = Ra_r/Ra$ when the two body forces are combined. For $F \to \infty$ the solution is identical to that of motions driven only by self-gravitation at comparable Ra_r, and conversely for $F \to 0$. Interesting flows are observed when the effects of the two forces are comparable. Such an effect is shown in Figure 7. The quasi-steady state solution in this figure was obtained in a rotating frame with $Ra = 10^5$, $Ra = 10^4$, $Re = 78{\cdot}4$, $Pr = 7$ and $\pi = 1$.

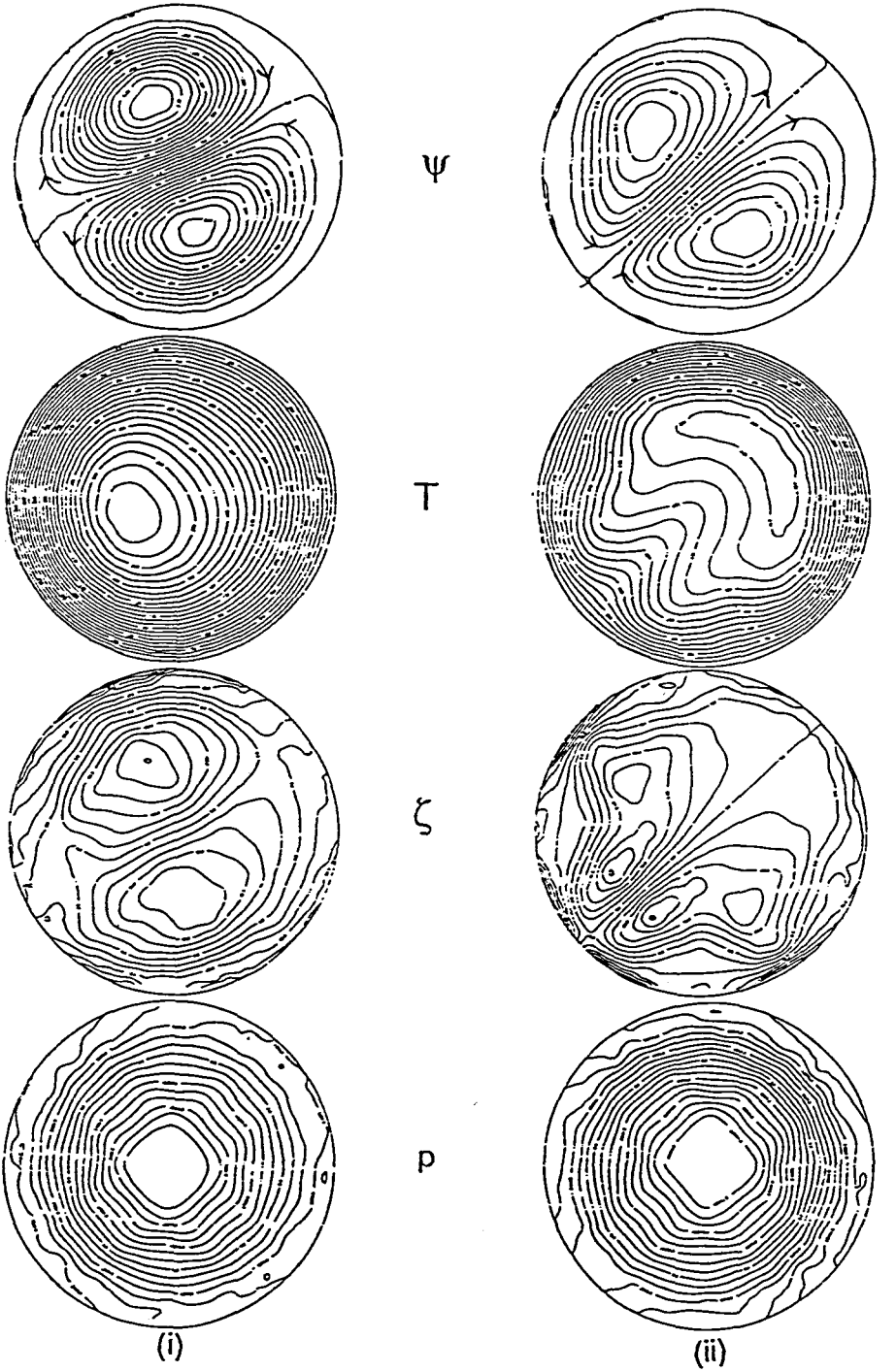

Figure 4. The effect of Rayleigh number Ra_r on the quasi-steady state thermal convection in an internally heated self-gravitating cylinder. Quasi-steady state solutions are provided in terms of contour maps of streamfunction ψ, temperature T, vorticity ζ and pressure p. Grid G201 was used.

(i) $Ra_r = 1{\cdot}66 \times 10^4$:
$\psi = -1{\cdot}3(0{\cdot}1)1{\cdot}3$, $T = 0(0{\cdot}01)0{\cdot}24$,
$\zeta = -30(5)40$, $p = -4000(500)3500$.

(ii) $Ra_r = 1 \times 10^5$:
$\psi = -5{\cdot}6(0{\cdot}8)6{\cdot}4$, $T = 0(0{\cdot}01)0{\cdot}16$,
$\zeta = -210(30)240$, $p = -18000(2000)18000$

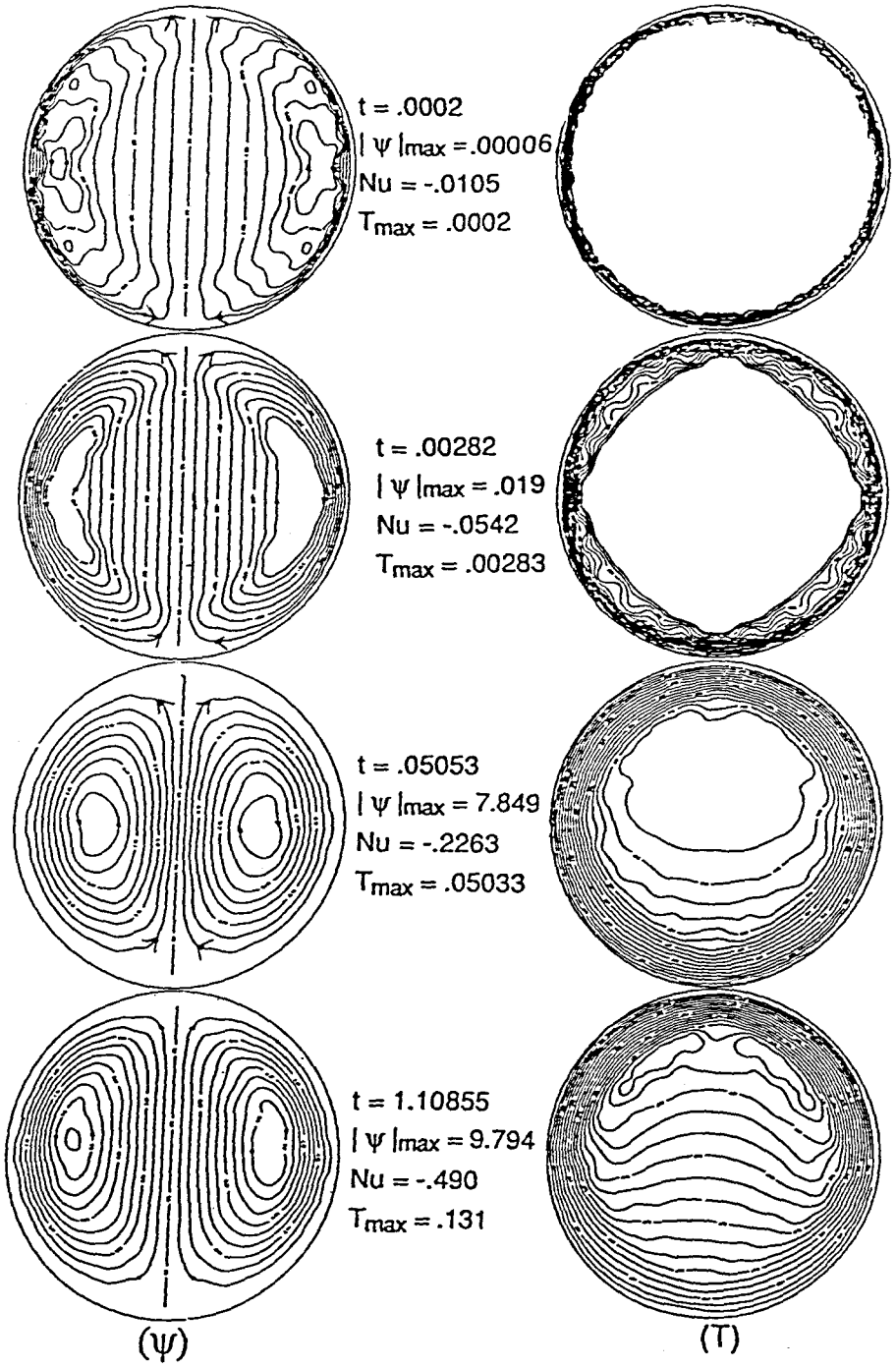

Figure 5. Time-dependent behaviour of motions driven by normal gravity field in an internally heated non-rotating cylinder. Results are given for $Ra = 10^5$, $Pr = 7{\cdot}0$ and $\pi = 1$. Note that the theoretical Nu at quasi-steady state is $-0{\cdot}5$ for all Ras (or Ra_rs). A value of $-0{\cdot}49$ is shown in this figure. Grid used is G449

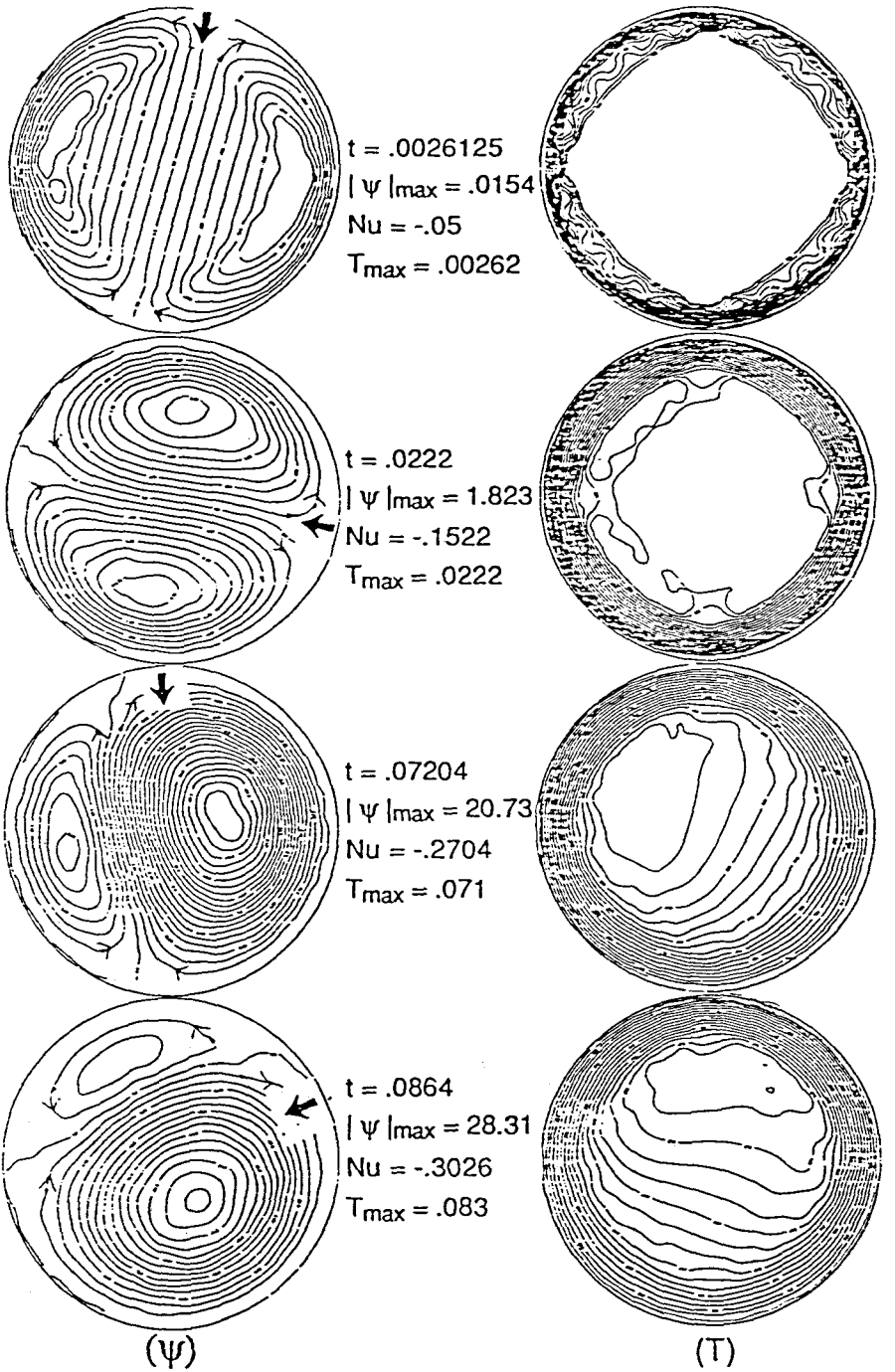

Figure 6. Motions driven by normal gravity in an internally heated rotating horizontal cylinder. Solutions are given in terms of a co-ordinate system that rotates with the cylinder, in which case the normal gravity field is oscillatory. The arrows on the boundary wall show the orientation of the normal gravity field as preceived by an observer at rest in the (counterclockwise) rotating frame of reference. To the observer in the rotating frame the normal, fixed gravity field appears to rotate in the clockwise direction. Results are for the point $Ra = 10^5$, $Re = 24{\cdot}7$, $Pr = 7{\cdot}0$ and $\pi = 1$ in the parameter space, and calculations were done with grid G449. An Re value 24·7 represents a fairly slow rotation

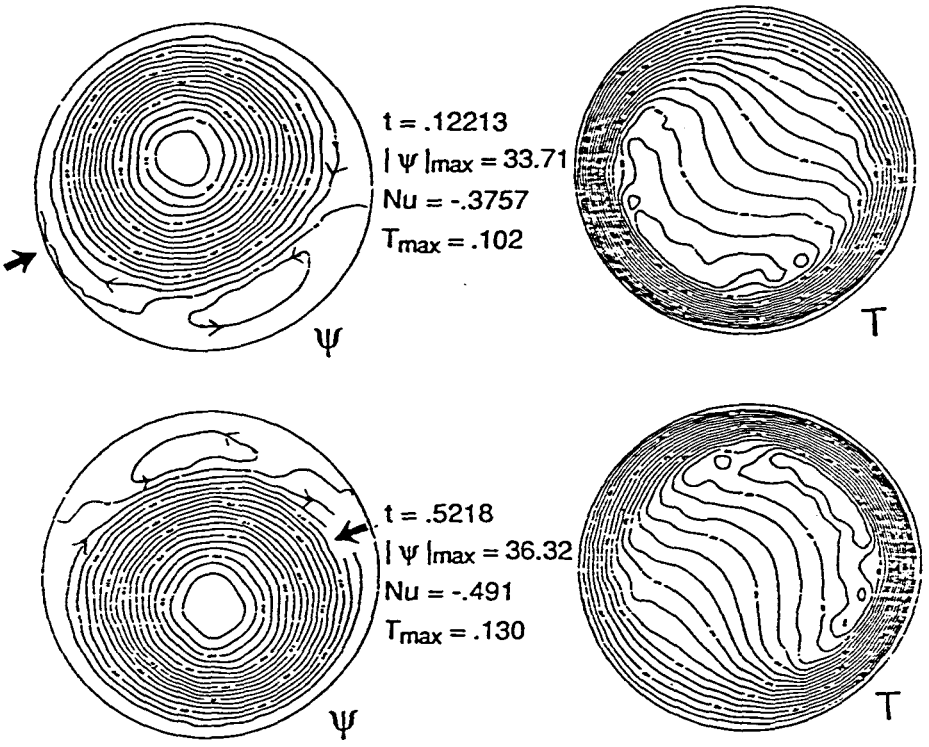

Figure 6. (Continued)

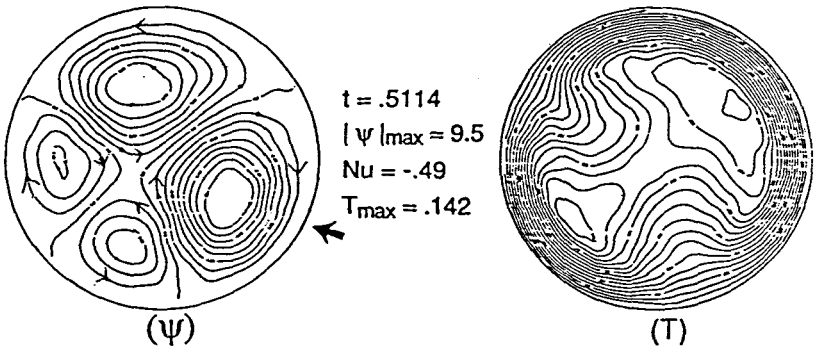

Figure 7. Convective motions observed when the normal gravity field is combined with self-gravitation in an internally heated cylinder. Quasi-steady state contour maps for streamfunction ψ and temperature T are shown in this figure. The results are for the point $Ra_c = 10^5$, $Ra = 78{\cdot}4$, $Pr = 7{\cdot}0$ and $\pi = 1$. Grid is G449

4.3. Sample results from the transient heating problem

The solutions obtained for the transient heating problem are in general very similar to those for internal heat generation. We provide Figure 8 to illustrate this fact. The figure shows the transient motion driven by normal gravity in a horizontal cylinder at $Ra = 10^5$. We see the similarity with those obtained in the internal heat generation problem in an inertial frame by comparing

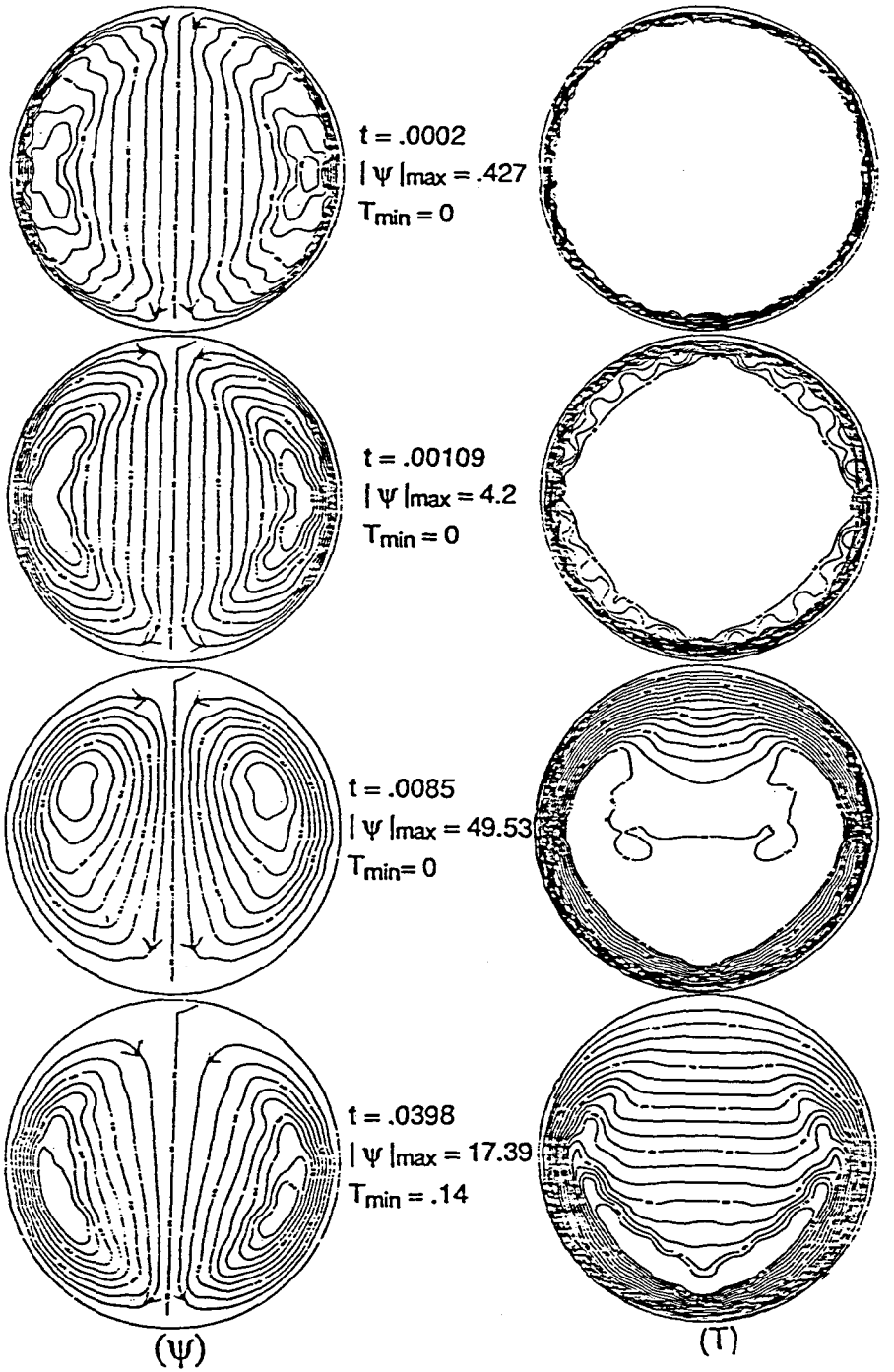

Figure 8. Transient behaviour of motions driven by normal gravity in non-rotating cylinder. The surface of the cylinder is heated by maintaining the surface at high temperature. Note that the initial and final conditions in the cylinder are characterized by zero velocities and by uniform dimensionless temperatures of 0 and 1 respectively. The results are for $Ra = 10^5$, $Pr = 7{\cdot}0$ and $\pi = 1$. Grid is G449

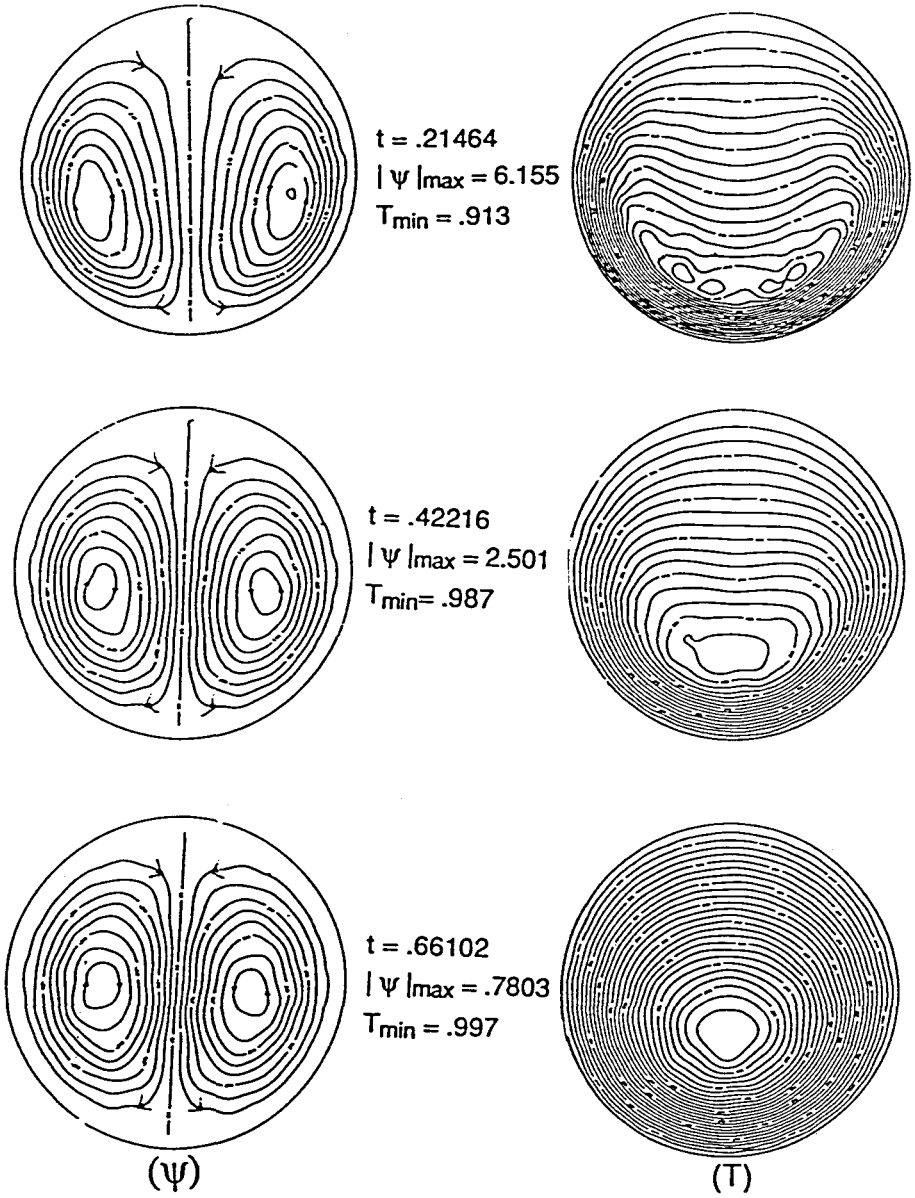

Figure 8. (Continued)

Figures 5 and 8. The sense of circulation of convection cells is of course reversed in the two problems since the 'basic' temperature gradients are in opposite directions. Note that while the final state of the flow is quasi-steady in the internal heat generation problem, the final state of the flow in the transient heating problem is motionless and isothermal at $T=1$. Also, more rigorous flows are found in the transient heating problem when compared with the internal heat generation problem.

Similar behaviours are observed in flows driven by centrifugal force (in the transient heating problem) when compared with flows driven by self-gravitation (in the internal heat generation problem). Of course, differences exist in the details of the flows in the two problems, these differences being due to the stronger motions and the fact that the temperature profile is significantly modified much earlier in the transient problem. For reasons of space we cannot give a detailed discussion of the 'non-numerical' aspects of the physics of the flows observed in the present study. Such discussions are provided in Ladeinde.[1] However, in the next section of the present paper we will discuss the computational difficulties encountered during the simulations.

5. COMPUTATIONAL ISSUES

We have found it appropriate to report on the major computational difficulties encountered during the present simulation. Some of the difficulties are not familiar in the finite element literature and are reported here for the records. As expected, the difficulties are more serious in large-amplitude flows. The numerical difficulties are discussed under the following headings: error-control scheme, minimum time of believability, quasi-Newton method, lower bound to minimum velocity, and manifestation of solution non-uniqueness by grid refinement.

5.1. Error-control scheme

We were very pleased with the error-control scheme for Ra (Ra_r) values below approximately 5×10^4 (10^5). In such cases the AB predictor was accurate so that only one Newton–Raphson iteration was necessary per time step. The scheme allowed very large time step sizes, resulting in a very 'fast' integration. In fact we observed a several thousand-fold increase in time step size at sufficiently low parameter values while ensuring a maximum time integration error of 0·2%.

At higher parameter values the step size Δt computed by the error-control scheme became unacceptably low (usually after approximately 35 time steps in most problems) so that the scheme became unattractive when compared with a constant-time-step-size integration with the backward Euler or the trapezoid rule. The foregoing difficulty might have been due to the accumulated round-off errors resulting from the non-dissipative trapezoid rule. (Double-precision arithmetic was used and the phenomenon was observed in all computing machines used, including IBM 4381 and VAX 750.) It is noted that the foregoing problem with the error-control scheme does not affect the accuracy of the solution.

The difficulty might also have been due to a combination of the round-off errors at higher parameter values and the relatively constant timescales associated with convection-dominated flows. Following a suggestion by P. M. Gresho (in a private communication) we implemented a 'restart' scheme in combination with the predictor–corrector method. We also implemented a scheme based on a forward Euler predictor and a backward Euler corrector for the same purpose. To implement the restart scheme we started the time integration 'afresh' after a preassigned number(s) of time steps (~ 35 in this study). With the restart scheme we effectively 'throw away' the accumulated round-off errors which otherwise pollute the determination of the predicted values, giving unreliably small Δt.

We have been satisfied with the restart scheme for $Ra \leq 5 \times 10^5$. The restart scheme also improved on the regular scheme for $Ra > 5 \times 10^5$, but computed Δts were still very low in this case and, in general, less cost-effective when compared with constant-step-size integration. The rate of increase of Δt with time for the predictor–corrector scheme based on the Euler formulae was too slow to recommend the method, and a constant-step-size integration with the backward Euler or the trapezoid rule (with backward Euler start) was used in cases where the 'regular' (or the 'restart') error-control scheme did not perform satisfactorily.

5.2. *Minimum time of believability*

The difficulty discussed in this subsection pertains to simulations using conventional Galerkin finite element methods for the transient Navier–Stokes or even the transient heat conduction equations in problems involving an abrupt change in Dirichlet boundary conditions.[36] The difficulty, which is mathematical in origin, was manifested in unphysical wiggles in the temperature field at short times in the transient studies. (Of course, no such difficulties were encountered in the heat generation problem.)

The wiggles in most of our simulations occurred only at a few mesh points, had negligible amplitudes at Ra, $Ra_r \leq 10^5$, and had a maximum amplitude less than 6% of T_{max} (depending on the grid) in the studies at Ra, $Ra_r = 10^6$. (T_{max} is the maximum temperature.) The wiggles in all studies disappeared before $t = 0{\cdot}02$ (i.e. 'the minimum time of believability' $\doteq 0{\cdot}02$). The solutions in most of our calculations are of acceptable accuracy (see some guidelines suggested by Gresho and Lee[36]). The exception is the simulation involving the combination of $Ra = 10^6$, $Ra_r = 10^6$, $Re = 7{\cdot}81$, $Pr = 7$ and $\pi = 1$. The velocities are very large in this case ($O(10^3)$) and very severe wiggles were observed at short times, the largest being 45% of T_{max}! The wiggles had disappeared by $t = 0{\cdot}0185$. Although the calculated results look physically reasonable, a finer grid than G649 is clearly needed for a more accurate resolution of the initial transients for this difficult problem. We emphasize that the time at whcih the wiggles disappear is fairly independent of the mesh or the flow strength (including pure conduction) for the range of parameters and computational grids studied.

5.3. *Quasi-Newton method*

We experimented with the quasi-Newton method[37, 38] as an alternative to the Newton–Raphson method for linearizing the equations for the corrector. We were not impressed with the performance of the quasi-Newton method when compared with one-step Newton–Raphson for the present simulations. This was because too many quasi–Newton iterations (up to 15 in some cases) were required per time step to obtain the convergence needed for the error-control method. The poor convergence might have resulted from the condensation procedure discussed earlier in this paper. In particular, the element centre nodes cannot contribute to the Jacobian matrix (or its inverse) during the 'quasi-Newton' iterations between refactoring steps. Similar concerns have been expressed by M. Engelman (in a private communication).

5.4. *Lower bound on minimum velocity*

The numerical difficulty discussed in this section was observed in the transient calculations for centrifugally driven flows in a rotating cylinder. Isothermal conditions ($T = 1$) and zero velocities are expected in the final state in this case. However, we observed a lower bound on the minimum velocity over the flowfield. That is, a 'residual' fluid motion was present at the final state, even though we had no trouble driving the temperature to a uniform field of value unity. The lower bound was considerably reduced by mesh refinements, however. For example, at $Ra_r = 10^5$ the (maximum) residual velocities obtained with G201, G449 and G649 were approximately 15, 5 and 3 respectively. The temperature field had reached the isothermal value of unity by this time. We attribute the behaviours to the inability of coarse grids to sufficiently resolve the spatial dependence of the centrifugal force field (since no such behaviours were found in flows driven by a normal gravity field). Also note that fluid viscosity is needed to dissipate the residual flow in the isothermal field, and dissipative numerical schemes could be very 'helpful' in this respect—we have used a non-dissipative time integration scheme for most of the time steps.

The present difficulty is reminiscent of the (strictly unrelated) one encountered by Leone[28] in the penalty Galerkin finite element simulation of steady state stratified flow across Owens valley. Leone reported some convergence limit beyond which the calculations would not go, so that the quadratic convergence of the Newton–Raphson technique was not realized. The exact cause was not known.

5.5. *Manifestation of solution non-uniqueness by grid refinement*

It is remarkable that all the grids shown in Figure 2 gave solutions with similar qualitative pictures for the range of parameter values studied and for all force fields. However, a very significant effect of grid refinement was observed on the accuracy of the solutions for flows driven by a self-gravitating (or centrifugal) force field, with differences up to 100% for G201 when compared with G649. The corresponding value for normal gravity-driven flows was usually less than 5%. Again, the spatial dependence of the forcing function terms is the probable cause.

The times at which mode transitions occurred (not shown) and the time required for the attainment of a quasi-steady state were heavily dependent on the grid in the studies on a self-gravitating cylinder. Another manifestation of insufficient grid points for spatial integration was the sense of circulation of the convection cells. The results obtained (at certain times during the transient) for $Ra_r = 10^5$ using G449 and G649 are shown in Figure 9. The difference between the

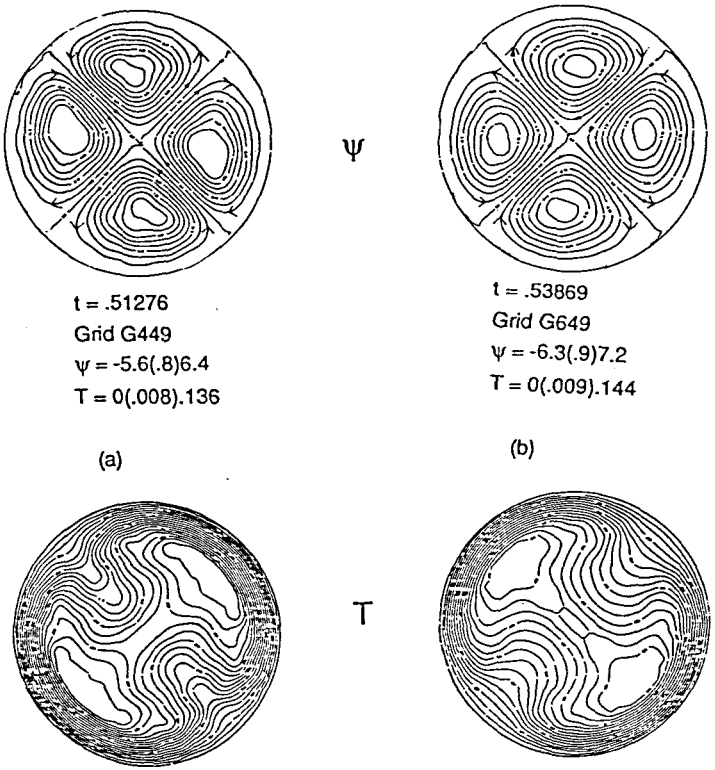

Figure 9. Non-uniqueness of quasi-steady solutions in motions driven by self-gravitation within a horizontal cylinder as manifested by grid refinement. Solutions are for $Ra_r = 10^5$. The results in this figure are analogous to the '2E' and '2P' solutions obtained by Weir[39] in his study of a self-gravitating sphere

two solutions in this figure is the sense of circulation, and identical convection modes can be obtained by simply rotating one of the patterns by 90°. The two convection patterns shown in Figure 9 are analogous to the so-called '2E' and '2P' (or vice versa, depending on the chosen reference axis) solutions obtained by Weir[39] in his study of self-gravitating spheres.

We believe that the occurrence of the two convection modes is a result of the interaction between the intrinsic arbitrariness (if unrestrained) in the azimuthal orientation of the convection cells and inaccurate spatial integration. The initial conditions (solutions) presumably play a decisive role in the orientation of the convection cells, and such initial conditions are affected by the parameter values and the accuracy (grid refinement) of integration.

6. CONCLUSIONS

In this paper we have discussed the performance of the penalty Galerkin finite element method when applied to a very complex time-dependent thermal convection problem involving rotation, self-gravitation and the normal external gravity field. The results have established the element method as a potentially valuable research/analytical tool in this or related areas. Moreover, the element method is very attractive for new problems such as the present one. This is because code validation can be done in 'loosely' related problems and in any geometry without a change in the solution algorithm. Also note that the singularity at the centre of the cylinder, which poses difficulties for the finite difference method,[8,40] does not require any special considerations in a finite element framework.

The difficulties encountered in large-amplitude flows in the present studies have been discussed, as were those associated with the oscillation of the normal gravity field. In retrospect, however, we feel that an explicit time integration scheme should have been used for those simulations involving a large frequency of oscillation of the normal gravity field (i.e. large Re) since the time step size must be very small. In this way we do not have to solve large matrices, and time step size restriction for stability will most likely be met, at least for the fully mixed non-penalty formulation.

Concerning the large amplitude of the short-time wiggles in studies with large parameter values, a cost-effective scheme might start the time integration with a relatively fine grid (e.g. via higher-order approximations) and switch to a coarser grid (lower-order approximation) after the minimum time of believability has been reached ($t \geq 0{\cdot}02$). The related method of adaptive grid refinement could also be used.

The foregoing proposals are currently being studied for implementation, as is a non-overlapping domain decomposition (i.e. block-by-block) method to permit the simulation of transient three-dimensional problems in computers with parallel processors. An intended application of the resulting code is the simulation of three-dimensional convection in rotating vertical cylinders with sloping ends. The latter model has found tremendous application in astrophysical fluid dynamics (see Busse and Or[41] and references therein).

ACKNOWLEDGEMENTS

We wish to express our sincere gratitude to Professor S. Leibovich of our department at Cornell University, Ithaca, New York for the discussions on physical and mathematical aspects of the present study. We are also grateful to Dr. P. M. Gresho of Lawrence Livermore Laboratory for his suggestions on certain numerical aspects of the study.

APPENDIX I

In this appendix we define the integrals associated with the matrices in equation (21). Towards this end we expand equation (21) as follows:

$$\begin{bmatrix} \frac{2}{\Delta t^l} M_{ij} + (Q_{ij} + R_{ij})^m + D(G^1_{ij} + G^2_{ij}) + \varepsilon C_{ij} + (T^1_{ij})^m & -AU_{ij} + DG^3_{ij} + \varepsilon D_{ij} + (T^2_{ij})^m & BX_{ij} + (-E)Z_{ij} \\ AV_{ij} + DH^1_{ij} + \varepsilon E_{ij} + (T^3_{ij})^m & \frac{2}{\Delta t^l} M_{ij} + (T^4_{ij})^m + (S_{ij} + T_{ij})^m + \varepsilon F_{ij} + D(H^2_{ij} + H^3_{ij}) & BY_{ij} - GZ_{ij} \\ (T^5_{ij})^m & (T^6_{ij})^m & \frac{2}{\Delta t^l} M_{ij} + (W_{ij})^m + P_{ij} \end{bmatrix} \begin{bmatrix} (\Delta u^{l+1}_j)^m \\ (\Delta v^{l+1}_j)^m \\ (\Delta T^{l+1}_j)^m \end{bmatrix}$$

$$= \begin{bmatrix} 2D\Theta^1_i - \left[\left(-\frac{2}{\Delta t^l} M_{ij} + (Q_{ij} + R_{ij}) + D(G^1_{ij} + G^2_{ij}) + \varepsilon C_{ij} \right) u^l_j + (-AU_{ij} + DG^3_{ij} + \varepsilon D^3_{ij}) v^l_j + [BX_{ij} + (-E)Z_{ij}] T^l_j \right] \\ 2D\Theta^2_i - \left[[AV_{ij} + DH^1_{ij} + \varepsilon E_{ij}] u^l_j + \left(-\frac{2}{\Delta t^l} M_{ij} + (S_{ij} + T_{ij}) + \varepsilon F_{ij} + D(H^2_{ij} + H^3_{ij}) \right) v^l_j + (BY_{ij} - GZ_{ij}) T^l_j \right] \\ 2Q^T_i - \left[\left(-\frac{2}{\Delta t^l} M_{ij} + W_{ij} + P_{ij} \right) T^l_j \right] \end{bmatrix}$$

$$- \begin{bmatrix} \left(\frac{2}{\Delta t^l} M_{ij} + (Q_{ij} + R_{ij})^m + D(G^1_{ij} + G^2_{ij}) + \varepsilon C_{ij} \right) u^{l+1}_j + (-AU_{ij} + DG^3_{ij} + \varepsilon D_{ij}) v^{l+1}_j + [BX_{ij} + (-E)Z_{ij}] T^{l+1}_j \\ (AV_{ij} + DH^1_{ij} + \varepsilon E_{ij}) u^{l+1}_j + \left(\frac{2}{\Delta t^l} M_{ij} + (S_{ij} + T_{ij})^m + \varepsilon F_{ij} + D(H^2_{ij} + H^3_{ij}) \right) v^{l+1}_j + (BY_{ij} - GZ_{ij}) T^{l+1}_j \\ \left(\frac{2}{\Delta t^l} M_{ij} + (W_{ij})^m + P_{ij} \right) T^{l+1}_j \end{bmatrix} \tag{24}$$

The matrices in equation (24) are

$$M_{ij} = \int_\Omega \phi_i \phi_j \, d\Omega, \qquad Q_{ij} = \int_\Omega \phi_i (u_I \phi_I) \frac{\partial \phi_j}{\partial x} d\Omega, \qquad R_{ij} = \int_\Omega \phi_i (v_I \phi_I) \frac{\partial \phi_j}{\partial y} d\Omega,$$

$$U_{ij} = M_{ij}, \qquad G^3_{ij} = \int_\Omega \frac{\partial \phi_i}{\partial y} \pi \frac{\partial \phi_j}{\partial x} d\Omega, \qquad X_{ij} = \int_\Omega \phi_i \phi_j \left(\sum_{k=1}^{L} x^k \phi'_k \right) d\Omega,$$

$$G^1_{ij} = 2 \int_\Omega \frac{\partial \phi_i}{\partial y} \pi \frac{\partial \phi_j}{\partial y} d\Omega, \qquad G^2_{ij} = \int_\Omega \frac{\partial \phi_i}{\partial y} \pi \frac{\partial \phi_j}{\partial y} d\Omega, \qquad D_{i\alpha} = C^1_{ij} [O_{\beta j}]^{-1} C^{2*}_{\beta\alpha} \quad \text{(see text)},$$

$$T^2_{ij} = u_k \int_\Omega \phi_i \phi_j \frac{\partial \phi_k}{\partial y} d\Omega, \qquad Z_{ij} = U_{ij}, \qquad C_{i\alpha} = C^1_{ij} [O_{\beta j}]^{-1} C^{1*}_{\beta\alpha},$$

$$T^1_{ij} = u_k \int_\Omega \phi_i \phi_j \frac{\partial \phi_k}{\partial x} d\Omega, \qquad V_{ij} = U_{ij}, \qquad H^1_{ij} = \int_\Omega \frac{\partial \phi_i}{\partial x} \pi \frac{\partial \phi_j}{\partial y} d\Omega,$$

$$T^4_{ij} = v_k \int_\Omega \phi_i \phi_j \frac{\partial \phi_k}{\partial y} d\Omega, \qquad Y_{ij} = \int_\Omega \phi_i \phi_j \left(\sum_{k=1}^{L} y^k \phi'_k \right) d\Omega, \qquad E_{i\alpha} = C^2_{ij} [O_{\beta j}]^{-1} C^{1*}_{\beta\alpha},$$

$$T^3_{ij} = v_k \int \phi_i \phi_j \frac{\partial \phi_k}{\partial x} d\Omega, \qquad S_{ij} = \int_\Omega \phi_i (u_\alpha \phi_\alpha) \frac{\partial \phi_j}{\partial x} d\Omega = Q_{ij}, \qquad T_{ij} = R_{ij},$$

$$F_{i\alpha}=C_{ij}^{2}[O_{\beta j}]^{-1}C_{\beta\alpha}^{2*}, \quad H_{ij}^{2}=\int_{\Omega}\frac{\partial\phi_i}{\partial x}\pi\frac{\partial\phi_j}{\partial x}\mathrm{d}\Omega, \quad H_{ij}^{3}=2\int_{\Omega}\frac{\partial\phi_i}{\partial y}\pi\frac{\partial\phi_j}{\partial y}\mathrm{d}\Omega,$$

$$T_{ij}^{5}=T_k\int_{\Omega}\phi_i\phi_j\frac{\partial\phi_k}{\partial x}\mathrm{d}\Omega, \quad T_{ij}^{6}=T_k\int_{\Omega}\phi_i\phi_j\frac{\partial\phi_k}{\partial y}\mathrm{d}\Omega, \quad W_{ij}=R_{ij}+Q_{ij},$$

$$P_{ij}=\int_{\Omega}\left(\frac{\partial\phi_i}{\partial x}\frac{\partial\phi_j}{\partial x}+\frac{\partial\phi_i}{\partial y}\frac{\partial\phi_j}{\partial y}\right)\mathrm{d}\Omega,$$

$$\Theta_i^1=\int_S\phi_i\left[2\pi\frac{\partial u}{\partial x}\eta_x+\pi\left(\frac{\partial u}{\partial y}+\frac{\partial v}{\partial x}\right)\eta_y\frac{-p}{D}\eta_x\right]\mathrm{d}S,$$

$$\Theta_i^2=\int_S\phi_i\left[\pi\left(\frac{\partial v}{\partial x}+\frac{\partial u}{\partial y}\right)\eta_x+2\pi\frac{\partial v}{\partial y}\eta_y-\frac{p}{D}\eta_y\right]\mathrm{d}S,$$

$$Q_i^{\mathrm{T}}=\int_S\phi_i\left(\frac{\partial T}{\partial x}\eta_x+\frac{\partial T}{\partial y}\eta_y\right)\mathrm{d}S+\int_{\Omega}\phi_i H\mathrm{d}\Omega.$$

APPENDIX II: NOMENCLATURE

d	as defined in equation (20)
$\mathbf{f}$	right-hand-side vector
F	Froude number, Ra_r/Ra
$\mathbf{g}$	gravity vector
g	absolute value of gravity vector
G	Gravitational constant
H	dimensionless volumetric heat generation
$\mathbf{i}$	unit vector in x-direction
$\mathbf{j}$	unit vector in y-direction
k	thermal conductivity
$\mathbf{k}$	unit vector in z-direction
$\mathbf{K}$	stiffness matrix
$\mathbf{M}$	mass matrix
$\mathbf{N}$	Newton–Raphson correction to stiffness matrix
Nu	Nusselt number
$\mathbf{O}$	origin of inertial and rotating co-ordinate frames
p	dimensionless reduced pressure
P	dimensional total pressure
Pr	Prandtl number
q	dimensionless wall heat flux
Q'''	dimensional volumetric heat generation
r	radial direction in polar co-ordinates
R	radius of cylinder or Reynolds number, depending on context
Ra	gravitational Rayleigh number
Ra_r	rotational or self-gravitational Rayleigh number
Re	rotational Reynolds number
t	dimensionless time or surface traction, depending on context
T	dimensionless temperature
$\mathbf{X}$	(x, y, z)

u	dimensionless velocity in X or x-direction
u_r	dimensionless velocity in r-direction
u_θ	dimensionless velocity in θ-direction
$\mathbf{u}$	$(u, v)^*$, $(u, v, w)^*$ or (u, v, T), depending on context
v	dimensionless velocity in Y or y-direction
w	dimensionless velocity in Z- or z-direction
X	x-direction in inertial Cartesian frame of reference
x	x-direction in rotating Cartesian frame of reference
Y	y-direction in inertial Cartesian frame of reference
y	y-direction in rotating Cartesian frame of reference
Z	z-direction in inertial Cartesian frame of reference
z	z-direction in rotating Cartesian frame of reference
ζ	axial vorticity
ψ	Stokes streamfunction
Ω	domain or angular velocity, depending on context
S	surface of Ω
π	viscosity ratio
Δt	time step size
ΔT	temperature difference $T - T_0$
$\overline{\Delta T}$	temperature difference $T_w - T_0$
ν	kinematic viscosity
α	thermal diffusivity
θ	azimuthal direction in polar co-ordinates
ρ	dimensional fluid density
ϕ_i	ith basis function for biquadratiitic Lagrange nine-node element
ϕ'_i	ith basis function for eight-node serendipity element
$\varepsilon', \varepsilon$	penalty parameter
ε_0	preset error limit
β	thermal expansion coefficient
η_i	ith component of the normal vector to a surface

Subscripts

m	iteration level
0	reference value, hydrostatic
p	predictor
w	wall
n	normal

Superscripts

l	time level
*	transpose
·	time derivative

REFERENCES

1. F. Ladeinde, 'Studies on thermal convection in self-gravitating and rotating horizontal cylinders in a vertical external gravity field', *Ph.D. Thesis*, Sibley School of Mechanical and Aerospace Engineering, Cornell University, 1988.

2. E. R. Benton and A. Clark, 'Spin-up', *Ann. Rev. Fluid Mech.*, **6**, 257–280 (1974).
3. S. Ostrach, 'Natural convection in enclosures', *Adv. Heat Transfer*, **8**, 161–227 (1972).
4. H. G. Maahs and M. M. David, 'Transient natural convection heat transfer on a horizontal cylinder', *Trends Eng.*, July, **20**(7), 8–20 (1968).
5. F. K. Deaver and E. R. G. Eckert, 'An interferometric investigation of convective heat transfer in a horizontal fluid layer with wall temperature increasing at a uniform rate', *Fourth Int. Heat Transfer Conf.*, Paris-Versailles, *Vol. IV-NC* 1, Elsevier, Amsterdam, 1970, pp. 1–12.
6. J. H. Van Sant, 'Free convection of heat-generating liquids in a horizontal pipe', *Nucl. Eng. Design*, **10**, 349–355 (1969).
7. M. Takeuchi and K. C. Cheng, 'Transient natural convection in horizontal cylinders with constant cooling rate', *Warme- und Stoffübertragung*, **9**, 215–225 (1976).
8. S. S. Leong and G. de Vahl Davis, 'Natural convection in a horizontal cylinder', *Report* 1979/*FMT*/5, presented at Int. Conf. on Numerical Methods in Thermal Problems, Swansea, 1979.
9. P. Bontoux, C. Smutek, B. Roux and J. M. Lacroix, 'Three-dimensional buoyancy-driven flows in cylindrical cavities with differentially heated endwalls', *J. Fluid Mech.*, **169**, 211–227 (1986).
10. P. M. Gresho, R. L. Lee and R. L. Sani, 'On the time-dependent solution of the incompressible Navier–Stokes equation in two and three dimensions', *Recent Advances in Numerical Methods in Fluids, Vol. 1*, in C. Taylor and K. Morgan (eds), Pineridge Press, Swansea, 1980, p. 27.
11. J. E. Hart, G. A. Glatzmaier and J. Toomre, 'Space-laboratory and numerical simulations of thermal convection in a rotating hemispherical shell with radial gravity', *J. Fluid Mech.*, **173**, 519–542 (1986).
12. S. Chandrasekhar, *Hydrodynamic and hydromagnetic stability*, 1st Edn, Dover, New York, 1961.
13. C. Tsuboi, *Gravity*, 1st Edn, George Allen and Unwin, Boston, MA, 1983.
14. F. H. Busse and C. R. Carrigan, 'Laboratory simulation of thermal convection in rotating planets and stars', *Science*, **19**, 81–83 (1976).
15. F. H. Busse, 'Non-linear properties of thermal convection', *Rep. Prog. Phys.*, **41**, 1930–1967 (1978).
16. P. M. Gresho, 'Contribution to Von Karman Institute lecture series on computational fluid dynamics: advection–diffusion and Navier–Stokes equations', *Report 92275*, Lawrence Livermore Laboratory, Livermore, CA, 1985.
17. M. Engelman, R. L. Sani, P. M. Gresho and M. Bercovier, 'Consistent vs reduced integration penalty methods for incompressible media using several old and new elements', *Int. j. numer. methods fluids*, **2**, 25–42 (1982).
18. O. C. Zienkiewicz, *The Finite Element Method*, 3rd Edn., McGraw-Hill, New York, 1977.
19. R. L. Sani, B. E. Eaton, P. M. Gresho, R. L. Lee and S. T. Chan, 'On the solution of the time-dependent incompressible Navier–Stokes equations via a penalty Galerkin finite element method', *Report 85354*, Lawrence Livermore Laboratory, Livermore, CA, 1981.
20. R. L. Sani, 'On the solution of the incompressible Navier–Stokes and Boussinesq equations via a penalty Galerkin finite element method', *Proc. Fourth Int. Symp. on Finite Element Methods in Flow Problems*, Tadahiko Kawai (ed), Publ. University of Tokyo Press, Tokyo, (1982), pp. 179–184.
21. E. L. Wilson, 'The static condensation algorithm', *Int. j. numer. methods eng.*, **8**, 198–203 (1973).
22. R. L. Lee, P. M. Gresho and R. L. Sani, 'Smoothening techniques for certain primitive varible solutions of the Navier–Stokes equations', *Int. j. numer. methods eng.*, **14**, 1785–1804 (1979).
23. R. S. Marshall, J. C. Heinrich and O. C. Zienkiewicz, 'Natural convection in a square enclosure by a finite element, penalty function method using primitive fluid variables', *Numer. Heat Transfer*, **1**, 315 (1978).
24. P. M. Gresho, R. L. Lee, R. L. Sani, M. K. Maslanik and B. E. Eaton, 'The consistent Galerkin FEM for computing derived boundary quantities in thermal and/or fluid problems', *Int. j. numer. method fluids*, **7**, 371–394 (1987).
25. M. Bercovier, M. Engelman, M. Fortin and N. Goldberger, 'Simulation of forming processes by FEM with a Bingham fluid model', *Int. j. numer. methods fluids*, **6**, 197–218 (1986).
26. J. N. Reddy, *An Introduction to the Finite Element Method*, 1st Edn, McGraw-Hill, New York, 1984.
27. V. Michelassi and C. Benocci, 'Solution of the steady state incompressible Navier–Stokes equations in curvilinear non-orthogonal coordinates', *Technical Note 158*, Von Karman Institute for Fluid Dynamics, Publ. Rhode Saint Genese, Belgium, 1986.
28. J. M. Leone, 'Finite element simulations of stratified flow over simple geometrical obstructions and arbitrarily complex terrain', *Ph.D. Thesis (Meteorology)*, Iowa State University, Ames, Iowa, 1980.
29. T. J. R. Hughes, W. K. Liu and A. Brooks, 'Finite element analysis of incompressible viscous flows by the penalty function formulation', *J. Comput. Phys.*, **30**, 1–60 (1979).
30. J. D. Hellums and S. W. Churchill, 'Computation of natural convection by finite difference', *Int. Heat Transfer Conf.* University of Colorado, Boulder, CO, Part V, Section B—Free convection, Paper 118, ASME, 1961, Publ. ASME, New York, pp. 985–994.
31. A. Sabsevari and S. Ostrach, 'Experimental studies of natural convection in a horizontal cylinder', *Proceedings of the Fifth Int. Heat Transfer Conference*, Tokyo, September 1974, Vol III-NC 3.4, Publ. ASME/AIchE, pp. 100–104.
32. P. M. Gresho, R. L. Lee, S. T. Chan and R. L. Sani, 'Solution of the time-dependent incompressible Navier–Stokes and Boussinesq equations using the Galerkin finite element method', *Lecture notes in Mathematics 771*, in A. Dold and B. Eckman, (eds), Springer, New York, 1980, pp. 203–221.
33. J. N. Reddy and A. Satake, 'A comparison of a penalty finite element model with the stream function–vorticity model of natural convection in enclosures', *J. Heat Transfer*, **102**, 659–666 (1980).
34. I. P. Jones and C. P. Thompson, 'Numerical solutions for a comparison problem on natural convection in an enclosed

cavity', *Report AERE-R9955*, United Kingdom Atomic Agency, Harwell, 1981.
35. G. de Vahl Davis, 'Natural convection of air in a square cavity: a bench mark numerical solution', *Int. j. numer. methods fluids*, **3**, 249–264 (1983).
36. P. M. Gresho and R. L. Lee, 'Don't suppress the wiggles—they're telling you something', *Comput. Fluids*, **9**, 223–253 (1980).
37. M. S. Engelman, G. Strang and J. Bathe, 'The applications of quasi-Newton methods in fluid mechanics', *Int. j. numer. methods eng.*, **17**, 707 (1981).
38. M. S. Engelman and R. L. Sani, 'Finite-element simulation of an *in*-package pasteurization process', *Numer. Heat Transfer*, **6**, 41 (1983).
39. A. D. Weir, 'Axisymmetric convection in a rotating sphere, Part 1: Stress-free surface', *J. Fluid Mech.*, **75**, 49–79 (1976).
40. R. J. Kee and A. A. Mckillup, 'A numerical method for predicting natural convection in horizontal cylinders with asymmetric boundary conditions', *Comput. Fluids*, **5**, 1–14 (1977).
41. F. H. Busse and A. C. Or, 'Convection in a rotating cylindrical annulus: thermal Rossby waves', *J. Fluid Mech.*, **166**, 173–187 (1986).